



HAL
open science

TVD-MOOD schemes based on implicit explicit time integration

Victor Michel-Dansac, Andrea Thomann

► **To cite this version:**

Victor Michel-Dansac, Andrea Thomann. TVD-MOOD schemes based on implicit explicit time integration. 2022. hal-02494767v4

HAL Id: hal-02494767

<https://hal.science/hal-02494767v4>

Preprint submitted on 26 Feb 2022 (v4), last revised 4 Jul 2022 (v6)

HAL is a multi-disciplinary open access archive for the deposit and dissemination of scientific research documents, whether they are published or not. The documents may come from teaching and research institutions in France or abroad, or from public or private research centers.

L'archive ouverte pluridisciplinaire **HAL**, est destinée au dépôt et à la diffusion de documents scientifiques de niveau recherche, publiés ou non, émanant des établissements d'enseignement et de recherche français ou étrangers, des laboratoires publics ou privés.

TVD-MOOD schemes based on implicit explicit time integration

VICTOR MICHEL-DANSAC¹
ANDREA THOMANN²

¹ Université de Strasbourg, CNRS, Inria, IRMA, F-67000 Strasbourg, France
Email address: victor.michel-dansac@inria.fr

² Institut für Mathematik, Johannes Gutenberg-Universität Mainz, Germany
Email address: athomann@uni-mainz.de.

Abstract. The context of this work is the development of first order total variation diminishing (TVD) implicit-explicit (IMEX) Runge-Kutta (RK) schemes as a basis of a Multidimensional Optimal Order detection (MOOD) approach to approximate the solution of hyperbolic multi-scale equations. A key feature of our newly proposed TVD schemes is that the resulting CFL condition does not depend on the fast waves of the considered model, as long as they are integrated implicitly. However, a result from Gottlieb et al. [17] gives a first order barrier for unconditionally stable implicit TVD-RK schemes and TVD-IMEX-RK schemes with scale-independent CFL conditions. Therefore, the goal of this work is to consistently improve the resolution of a first-order IMEX-RK scheme, while retaining its L^∞ stability and TVD properties. In this work we present a novel approach based on a convex combination between a first-order TVD IMEX Euler scheme and a potentially oscillatory high-order IMEX-RK scheme. We derive and analyse the TVD property for a scalar multi-scale equation and numerically assess the performance of our TVD schemes compared to standard L -stable and SSP IMEX RK schemes from the literature. Finally, the resulting TVD-MOOD schemes are applied to the isentropic Euler equations in two dimensions.

Keywords. MOOD, L^∞ stability, TVD schemes, IMEX RK schemes, isentropic Euler equations.

2020 Mathematics Subject Classification. 65M06, 65M08, 65M12 .

1. Introduction

Multi-scale equations arise in a wide range of applications, such as shallow flows studied e.g. in [4], magnetohydrodynamics [29], multi-material interfaces [1] or atmospheric flows [27]. When developing numerical methods for such applications, it is of prime importance to obtain physically admissible solutions under these multi-scale constraints. In order to numerically treat these different scales, one must assess whether the fast scales are relevant to the physical solution. Indeed, accurately capturing these fast scales requires a very restrictive time step. This issue is discussed e.g. in [18] for the Euler equations. When the impact of the fast scales on the physical solution is less important, numerical methods that do not accurately capture all scales, but only follow the slow dynamics, are necessary. One option, which we will study in this paper, is to use Implicit-Explicit (IMEX) schemes, where the terms associated to the fast wave propagation are treated implicitly. Such schemes are well-studied in the literature, see for instance [3] for efficient IMEX schemes applied to hyperbolic-parabolic problems, [36] for IMEX schemes adapted to stiff relaxation source terms, or [34, 12, 5] for IMEX schemes designed for the low Mach regime of the Euler equations, as well as the references given therein. In this work, we are concerned with hyperbolic systems whose stiffness comes from the flux, rather than a source term. Let us emphasise that we will not consider hyperbolic systems with stiff source terms typically arising from relaxation processes. For their treatment, we refer for instance to [36].

To increase the quality of numerical approximations, one may turn to high-order schemes. However, such schemes are known to introduce spurious oscillations in the solution away from smooth regions.

This work has been partially funded by a CNRS-INSMI PEPS JCJC project.
A.T. has been partially supported by the Gutenberg Research College, JGU Mainz.

This is an issue, especially when considering non-linear hyperbolic equations, as the solution can develop discontinuities even when starting with a smooth initial condition. This was already observed by Harten in [19], who introduced the notion of total variation diminishing (TVD) schemes, and constructed non-oscillatory explicit and implicit second-order TVD schemes. Those schemes are non-linear, even when applied on linear equations, as from Godunov’s theorem follows that linear TVD schemes can only be first-order accurate [13]. Since non-linear implicit schemes are computationally very costly, especially when applied to non-linear systems of equations, the construction of higher order explicit TVD schemes remained an active area of research, see e.g. [42, 39, 16, 7] and references therein. Later, in the more general framework of strong stability preserving (SSP) implicit and explicit schemes [17], the stability property is achieved by relying on convexity arguments regarding forward and backward Euler schemes, rather than adding artificial viscosity to achieve the TVD property, as was done in [19, 42, 37]. The high-order explicit and implicit SSP schemes developed in [17, 14, 15] have a CFL restriction of the order of the CFL restriction of a forward Euler scheme in order to remain oscillation-free. This makes the use of high-order implicit SSP schemes rather costly and impractical in applications compared to high-order explicit SSP schemes, as was remarked in [15]. Regarding IMEX SSP schemes, we refer for instance to [22, 9, 23]. All high-order SSP schemes mentioned above require the time step to depend on all scales to achieve stability, but are provably high-order accurate. Unfortunately, they are not well suited for the multi-scale setting, where the time step is strongly restricted by the fast scale leading, in extreme cases, to a vanishing time step.

In contrast, our focus here is the construction of first order IMEX TVD schemes, which have a CFL restriction that solely stems from the explicitly treated terms associated to a scale-independent material velocity. The work presented in this manuscript is greatly motivated by the seminal work by Gottlieb et al. [17], where it was proven that an unconditionally TVD implicit RK scheme is at most first-order accurate, see also [41, 21]. Unfortunately, this result holds also for IMEX discretisations with a scale-independent CFL restriction. In fact, this discouraging result is also observed in [11, 6] when attempting to construct second-order TVD IMEX schemes for the Euler equations.

Although the TVD property is crucial to accurately capture discontinuities in the numerical solution, its importance decreases in smooth regions. In order to achieve a high-order approximation of the solution in such regions, while keeping the solution as oscillation-free as possible in the vicinity of discontinuities, we adapt to the IMEX framework a procedure inspired from the MOOD (Multidimensional Optimal Order Detection) techniques from [8]. The gist of the MOOD framework is to lower the order of accuracy of the scheme near problematic zones, i.e. zones where the high-order scheme violates some predetermined admissibility constraint. Therefore, a lower order scheme with good stability properties, called a *parachute scheme*, is needed in the MOOD framework.

In the present work, as stated before, we design first-order TVD IMEX RK discretisations that have a higher resolution than the standard first-order backward/forward Euler (IMEX1) scheme. Such discretisations therefore provide suitable fall-back schemes for the MOOD approach, yielding a reduced space-time error compared to using a traditional IMEX1 scheme as a parachute. The approach given here to construct such a fall-back scheme builds on the results from [11, 33], where the increase in precision was achieved by introducing a convex combination of said first-order TVD scheme with an oscillatory second-order scheme. In [11], the ARS(2,2,2) scheme from [3] was used as a basis for the convex combination, and this result was extended to a general class of second-order IMEX RK schemes in [33]. Here, we generalize and extend the results from [11, 33] even further, applying a convex combination to each stage, rather than merely to the final update as done in [11, 33]. This allows to construct TVD schemes based on arbitrarily high order Butcher tableaux. Note that convex combinations have already been used to recover first-order properties lost at higher orders, see for instance [24] to recover the positivity property or [31] for well-balanced problems.

The paper is organised as follows. In Section 2, we motivate the problem of multi-scale equations, illustrated by a scalar linear transport equation. We also introduce notation for the space discretisation.

TVD-MOOD SCHEMES

Section 3 revisits the MOOD procedure and details the construction of the numerical scheme. The formalism of IMEX-RK is briefly recalled and the TVD constraints are derived for the time-semi discrete scheme. Subsequently, the fully discrete scheme is given, based on a finite volume approach and TVD limiters. To completely determine the scheme, the choice of free parameters in the convex combinations is addressed. Section 4 is devoted to numerical experiments to verify the properties of the parachute first order TVD scheme as well as the MOOD scheme. To numerically validate that our TVD-IMEX-MOOD schemes are a noticeable improvement over widely used L -stable IMEX and the SSP IMEX schemes, we compare the performance of the schemes in terms of accuracy, CPU times and CFL restrictions on discontinuous solutions of the scalar multi-scale equation. Moreover, we show numerically that using our TVD scheme as a basis of the MOOD procedure shows a significant reduction of the space-time error. We finally apply the scheme to the isentropic Euler equations, assessing its performance for Riemann problems in one and two space dimensions, as well as its accuracy. To complete this manuscript, a conclusion is presented in section 5.

2. Motivation

To study conditions to obtain a TVD scheme, we consider the linear advection equation

$$\begin{cases} w_t + c_m w_x + \frac{c_a}{\varepsilon} w_x = 0, \\ w(0, x) = w^0(x), \end{cases} \quad (2.1)$$

where $w : (\mathbb{R}^+, \Omega) \rightarrow \mathbb{R}$, $\Omega \subset \mathbb{R}$. In (2.1), c_m and c_a/ε denote two transport speeds which can differ significantly depending on the choice of the parameter $\varepsilon > 0$. Without loss of generality, we consider only positive transport directions, i.e. $c_m > 0$ and $c_a > 0$. In the following, we consider $c_m = \mathcal{O}(1)$ and $0 < c_a/\varepsilon \leq c_m$. The term $\frac{c_a}{\varepsilon} w_x$ is stiff as soon as $\varepsilon \ll 1$, and applying a purely explicit scheme would lead to a severe time step restriction, given by

$$\Delta t \leq \varepsilon \mathcal{C} \frac{\Delta x}{\varepsilon c_m + c_a},$$

with a CFL coefficient \mathcal{C} independent of ε . However, when ε tends to zero, the above time step would vanish, which would lead to huge computational costs, especially when considering long time periods. Therefore, to avoid such a restriction, we integrate the wave associated to c_a/ε implicitly, whereas $c_m w_x$ is treated explicitly. This approach leads to a CFL condition oriented to the slow wave c_m , independently of ε . It is given by

$$\Delta t \leq \tilde{\mathcal{C}} \frac{\Delta x}{c_m}. \quad (2.2)$$

In space, we use an upwind discretization since it was shown in [12] that the use of centred differences destroys the L^∞ stability for non-linear systems. Even though our considered problem is linear, the goal is to apply the scheme on non-linear systems such as the isentropic Euler equations discussed in Section 4.2.

The space and time discretisations follows the usual finite volume framework, where the computational domain Ω is divided in N uniformly spaced cells $C_j = (x_{j-1/2}, x_{j+1/2})$, of size Δx and whose center is $x_j = j\Delta x$. The solution in cell C_j is then approximated by the cell average, given by

$$w_j(t) \approx \frac{1}{\Delta x} \int_{\Omega_j} w(x, t) dx. \quad (2.3)$$

A first order space semi-discrete scheme

approximating weak solutions to (2.1) is then given by

$$\partial_t w_j(t) + \frac{c_m}{\Delta x} \Delta_j(t) + \frac{c_a}{\varepsilon \Delta x} \Delta_j(t) = 0, \quad (2.4)$$

where we have introduced the abbreviation $\Delta_j(t) = w_j(t) - w_{j-1}(t)$. To obtain a fully discrete scheme, a suitable implicit-explicit time integration method has to be applied. We discretise the time variable with $t^{n+1} = t^n + \Delta t$, where Δt denotes the time step and has to obey a material CFL condition (2.2). However, it is well known, see e.g. [17], that approximating discontinuous solutions with high-order non-TVD methods can lead to spurious artefacts near jump positions. This behaviour is illustrated in Figure 1, where we display the approximation of an advected rectangular bump profile with the first-order scheme

$$w_j^{n+1} = w_j^n - \lambda \Delta_j^n - \mu_\varepsilon \Delta_j^{n+1}, \quad (2.5)$$

as well as with the well-known second-order ARS(2,2,2) and third-order ARS(2,3,3) IMEX schemes from [3]. The details on the numerical experiment are given in Section 4. We clearly observe in Figure 1 that the ARS methods violate the bounds on the numerical solution in both cases. Therefore, in order to avoid oscillations as in Figure 1, we need L^∞ stable or TVD schemes. Here, a scheme is said to be L^∞ stable if

$$\|w^{n+1}\|_\infty = \max_{j \in \{1, \dots, N\}} |w_j^{n+1}| \leq \|w^n\|_\infty, \quad (2.6)$$

and TVD if

$$\text{TV}(w^{n+1}) = \sum_{j=1}^N |w_{j+1}^{n+1} - w_j^{n+1}| \leq \text{TV}(w^n). \quad (2.7)$$

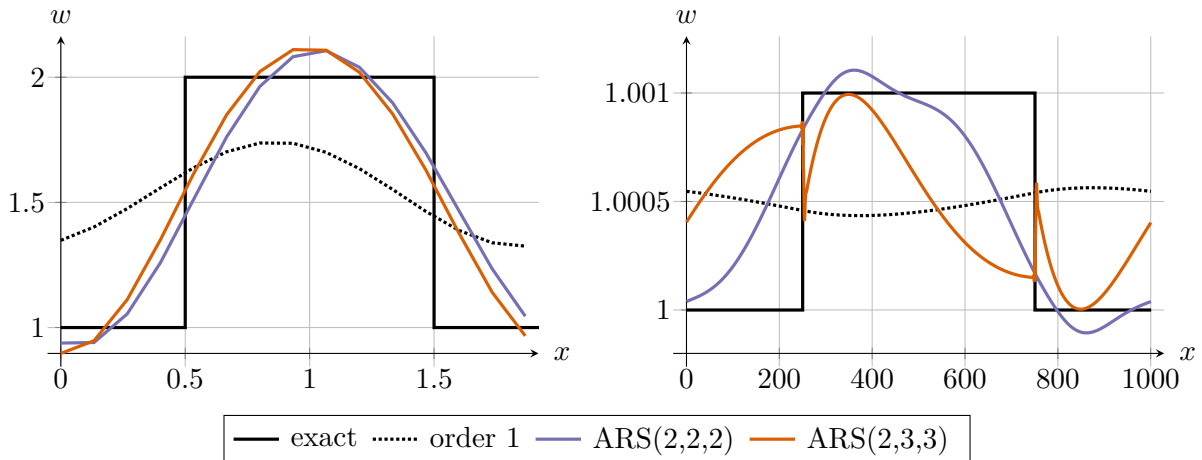


FIGURE 1. Approximation of a discontinuous solution using the first-order, second-order ARS(2,2,2) and third-order ARS(2,3,3) schemes. Left panel: $\varepsilon = 1$ and $N = 15$; right panel: $\varepsilon = 10^{-3}$ and $N = 2000$; see Section 4 for more information on the test case.

Unfortunately, it can be proven for IMEX RK schemes, following a result of Gottlieb et al. [17], that there cannot exist L^∞ stable IMEX RK schemes of order $p \geq 2$ whose CFL restriction only stems from the explicitly treated part. Therefore, it does not make sense to look for higher order TVD IMEX integrators. However, we clearly see in Figure 1 that the first-order scheme is too diffusive to capture the structure of the solution, and thus it is also not a good choice as a base scheme in the MOOD hierarchical structure. As a consequence, our main focus here is to construct a first-order IMEX integration scheme fulfilling the L^∞ stability (2.6) and TVD property (2.7), that has a reduced numerical diffusion compared to the first order scheme (2.5), and is therefore suited as a fallback scheme when combined with a MOOD procedure.

3. Derivation of the numerical scheme

The goal of this section is the derivation of a numerical scheme based on a MOOD-like procedure. The usual MOOD framework for explicit schemes, see e.g. [8], consists in locally and gradually lowering the order of the scheme when an oscillation is detected. In our case, the lowest order scheme consists of a first order TVD-IMEX scheme. Is also referred to as *parachute* scheme since, generally speaking, it guarantees the preservation of desired properties once the high order scheme violates some predetermined condition. Here, the higher order scheme is given by a standard IMEX-RK scheme. Consequently, the precision of the first order TVD scheme can be improved without degrading its stability properties, yielding a high order approximation in smooth flow regimes. Due to the non-local nature of the implicit part in the IMEX schemes, the standard MOOD algorithm as given in [8] has to be modified, since the solution cannot be recomputed on a few selected cells only. Therefore, it has to be updated on the whole mesh.

Depending on the application, different detection criteria can be applied to identify oscillations violating the TVD property. For the toy problem (2.1), an oscillation is detected when the solution leaves the bounds of the initial condition. Indeed, the unknown w for this toy problem satisfies the maximum principle $\partial_t \|w(t, x)\|_\infty \leq 0$ (the equality is even verified), and therefore an L^∞ -stable discretisation obeys $\|w^{n+1}\|_\infty \leq \|w^0\|_\infty$ for all $n \geq 0$. For the isentropic Euler equations, a nonlinear system of hyperbolic conservation laws, this criterion needs to be modified since the maximum principle does not hold in general for all variables. However, as stated in [40], when considering a Riemann problem, at least one Riemann invariant satisfies a maximum principle from which a detection criterion can be formulated. Thus, detection criteria depend on the initial condition and are detailed in section 4, devoted to numerical experiments. In the remainder of this section, we denote by Φ a detection criterion suited to the problem under consideration.

The modified MOOD scheme, see also [11, 33], is given by the following algorithm.

Algorithm 1 (MOOD $_p$ scheme). *Define the initial detection criterion given by $\mathcal{E}^0 = \|\Phi(w^0)\|$. Equipped with a stable first order TVD scheme, the MOOD $_p$ scheme consists of applying the following procedure at each time step:*

- (1) *Compute a candidate numerical solution w_c^{n+1} with a p^{th} order IMEX-RK scheme.*
- (2) *Detect whether an oscillation is present somewhere in the space domain, i.e. whether the detection criterion is satisfied by the candidate solution:*

$$\|\Phi(w_c^{n+1})\|_\infty \leq \mathcal{E}^n. \tag{DMP}$$

- (3a) *If (DMP) holds, set for the numerical solution at the new time step $w^{n+1} = w_c^{n+1}$.*
- (3b) *Otherwise, compute a solution w_{\clubsuit}^{n+1} with the parachute scheme and set $w^{n+1} = w_{\clubsuit}^{n+1}$.*
- (4) *For a time-dependent detection criterion, update $\mathcal{E}^{n+1} = \xi \|\Phi(w^{n+1})\|_\infty + (1-\xi)\mathcal{E}^n$ with $\xi \in [0, 1]$, otherwise set $\mathcal{E}^{n+1} = \mathcal{E}^0$.*

Note that, in Step (4) of the above MOOD algorithm, the detection criterion is relaxed with a convex combination of parameter $\xi \in [0, 1]$ between the current solution and the criterion at the previous time step. This allows a finer control of the permitted oscillations in the MOOD solution.

A crucial part of the MOOD scheme is the construction of the parachute scheme, which should preserve the TVD property of the solution in case the higher order scheme produces oscillations. This is addressed in the following section.

3.1. Construction of the time-semi discrete parachute scheme

The proposed parachute schemes are based on an IMEX-RK approach where the implicit part is diagonally implicit. The time update for an s -stage IMEX-RK scheme for equation (2.4) is given by

$$w_j^{n+1} = w_j^n - \lambda \sum_{k=1}^s \tilde{b}_k \Delta_j^{(k)} - \mu_\varepsilon \sum_{k=1}^s b_k \Delta_j^{(k)}, \quad (3.1)$$

where we have set

$$\lambda = \frac{\Delta t}{\Delta x} c_m, \quad \mu_\varepsilon = \frac{\Delta t}{\Delta x} \frac{c_a}{\varepsilon}, \quad \Delta_j^{(k)} = w_j^{(k)} - w_{j-1}^{(k)},$$

and where the stages are defined as

$$w_j^{(k)} = w_j^n - \lambda \sum_{l=1}^{k-1} \tilde{a}_{kl} \Delta_j^{(l)} - \mu_\varepsilon \sum_{l=1}^k a_{kl} \Delta_j^{(l)}. \quad (3.2)$$

For the sake of clarity, we consider an IMEX-RK method of type CK (Carpenter and Kennedy) [25], i.e. we take $a_{11} = 0$. For results based on a non-CK scheme, with $a_{11} \neq 0$, see Appendix B. In order to obtain a CFL condition like (2.2), which does not depend on ε , the weights $(a_{k1})_{k \in \{2, \dots, s\}}$, as well as b_1 , have to be zero. This was shown in detail in [33] for a generic second-order CK method. We summarize the structure of the RK scheme in the following Butcher tableaux notation

$$\begin{array}{c|cccc} & 0 & 0 & \cdots & 0 \\ \tilde{c}_2 & \tilde{a}_{21} & 0 & \cdots & 0 \\ \text{explicit: } \vdots & \vdots & \ddots & \ddots & \vdots \\ \tilde{c}_s & \tilde{a}_{s1} & \cdots & \tilde{a}_{s,s-1} & 0 \\ \hline & \tilde{b}_1 & \cdots & \tilde{b}_{s-1} & \tilde{b}_s \end{array} \quad \text{implicit: } \begin{array}{c|cccc} & 0 & 0 & \cdots & 0 \\ c_2 & 0 & a_{22} & \cdots & 0 \\ \vdots & \vdots & \vdots & \ddots & \vdots \\ c_s & 0 & a_{s2} & \cdots & a_{ss} \\ \hline & 0 & b_2 & \cdots & b_s \end{array}, \quad (3.3)$$

with the coefficients \tilde{c} and c obeying

$$\tilde{c}_i = \sum_{j=1}^{i-1} \tilde{a}_{ij} \quad \text{and} \quad c_i = \sum_{j=1}^i a_{ij}. \quad (3.4)$$

Since the TVD scheme we construct are based on higher order IMEX-RK schemes, the weights have to fulfil high-order compatibility conditions as given in [35]. For orders higher than three, we refer to the order conditions in [25].

To obtain a TVD scheme from an s -stage IMEX-RK scheme, we propose a convex combination of each stage with the first-order IMEX Euler scheme (2.5) at time $t^n + c_k \Delta t$ for the k^{th} stage. This approach yields s free parameters $\theta_k \in [0, 1]$, where $k = 1, \dots, s$ denotes the stage in the IMEX scheme. The closer each θ_k is to 1, the higher the contribution of the IMEX-RK scheme. Consequently, we shall seek to maximize the values of θ_k to reduce diffusion as much as possible compared to the first order IMEX Euler scheme.

In this framework, the stages of the TVD scheme are defined by

$$w_j^{(k)} + (1 - \theta_k) c_k \mu_\varepsilon \Delta_j^{(k)} = w_j^n - \lambda \left((1 - \theta_k) \tilde{c}_k \Delta_j^n + \theta_k \sum_{l=1}^{k-1} \tilde{a}_{kl} \Delta_j^{(l)} \right) - \mu_\varepsilon \theta_k \sum_{l=1}^k a_{kl} \Delta_j^{(l)}. \quad (3.5)$$

and the update by

$$w_j^{n+1} = w_j^n - \theta_{s+1} \left(\lambda \sum_{k=1}^s \tilde{b}_k \Delta_j^{(k)} + \mu_\varepsilon \sum_{k=1}^s b_k \Delta_j^{(k)} \right) - (1 - \theta_{s+1}) \left(\lambda \Delta_j^n + \mu_\varepsilon \Delta_j^{n+1} \right). \quad (3.6)$$

TVD-MOOD SCHEMES

Note that, for the Butcher tableaux in the manner of (3.3), we immediately set $\theta_1 = 1$ to recover $w^{(1)} = w^n$. This means the convex stages appear earliest for $k = 2$. In the case where the weights \tilde{b} and b coincide with the last row of \tilde{A} and A , respectively, the stage $w^{(s)}$ coincides with the final update w^{n+1} . In particular, we then have $\theta = \theta_s$.

We emphasise that a TVD scheme resulting from the convex combination (3.6) is at most first-order accurate, see for instance [41, 17, 21]. However, it is a great fit as a parachute scheme for the MOOD algorithm 1. In section 3.1.1, we illustrate the procedure on how to obtain necessary conditions on the free parameters respecting the TVD property using a three stage IMEX-RK scheme. Then, in section 3.1.2, we state an extension to construct TVD discretisations based on the general form (3.3).

3.1.1. TVD conditions for a three stage scheme

As basis of the TVD scheme, we consider Butcher tableaux with $s_{\text{eff}} = 3$ effective computational steps. In the spirit of (3.3), they are given by

$$\text{explicit: } \begin{array}{c|ccc} 0 & 0 & 0 & 0 \\ c_2 & \tilde{a}_{21} & 0 & 0 \\ c_3 & \tilde{a}_{31} & \tilde{a}_{32} & 0 \\ \hline & 0 & b_2 & b_3 \end{array}, \quad \text{implicit: } \begin{array}{c|ccc} 0 & 0 & 0 & 0 \\ c_2 & 0 & a_{22} & 0 \\ c_3 & 0 & a_{32} & a_{33} \\ \hline & 0 & b_2 & b_3 \end{array}. \quad (3.7)$$

Therein, we have assumed that $\tilde{b} = b$ and $\tilde{c} = c$, see also [36]. This has the advantage that the weights in the final update coincide with respect to the explicitly and implicitly treated terms.

Applying the third-order conditions as given in [35] on the weights and coefficients given by (3.7) leads to the following tableaux, with $\gamma \notin \{0, \frac{1}{3}\}$:

$$\text{explicit: } \begin{array}{c|ccc} 0 & 0 & 0 & 0 \\ \frac{3\gamma-1}{6\gamma} & \frac{3\gamma-1}{6\gamma} & 0 & 0 \\ \frac{\gamma+1}{2} & -\frac{6\gamma^3-3\gamma^2+1}{2(3\gamma-1)} & \frac{\gamma(3\gamma^2+1)}{3\gamma-1} & 0 \\ \hline & 0 & \frac{3\gamma^2}{3\gamma^2+1} & \frac{1}{3\gamma^2+1} \end{array}, \quad \text{implicit: } \begin{array}{c|ccc} 0 & 0 & 0 & 0 \\ \frac{3\gamma-1}{6\gamma} & 0 & \frac{3\gamma-1}{6\gamma} & 0 \\ \frac{\gamma+1}{2} & 0 & \gamma & \frac{1-\gamma}{2} \\ \hline & 0 & \frac{3\gamma^2}{3\gamma^2+1} & \frac{1}{3\gamma^2+1} \end{array}. \quad (3.8)$$

We now demonstrate that, using Butcher tableaux (3.8), a first order TVD scheme can be obtained. First, we show the L^∞ stability (2.6), i.e. $\|w^{n+1}\|_\infty \leq \|w^n\|_\infty$. The idea of the proof lies in estimating the L^∞ norm of each stage against $\|w^n\|_\infty$, which will then be used to obtain the final estimate (2.6). The proof can be achieved by only applying the triangle and reverse triangle inequality. For clarity, we do not replace the coefficients of the tableaux by their γ -dependent values yet.

The first stage reduces to $w^{(1)} = w^n$ and we trivially obtain $\|w^{(1)}\|_\infty = \|w^n\|_\infty$. Furthermore, $w^{(1)}$ is independent of θ_1 , and therefore we can set $\theta_1 = 1$. Note this reasoning applies to any tableau that falls within the general form (3.3), and thus that such tableaux always allow to take $\theta_1 = 1$.

The second stage is given as follows, by (3.5):

$$w_j^{(2)} + a_{22}\mu_\varepsilon\Delta_j^{(2)} = w_j^n - \lambda \left((1 - \theta_2)a_{22}\Delta_j^n + \theta_2\tilde{a}_{21}\Delta_j^n \right).$$

Reformulating and collecting terms in w_j^n, w_{j-1}^n , and using that $\tilde{a}_{21} = a_{22}$, we obtain the following expression

$$w_j^{(2)} + a_{22}\mu_\varepsilon\Delta_j^{(2)} = (1 - \lambda a_{22}) w_j^n + \lambda a_{22} w_{j-1}^n. \quad (3.9)$$

Note that the second stage, like the first one, is independent of θ_2 . Thus, we can set $\theta_2 = 1$, which achieves the full contribution of the second stage of the IMEX-RK scheme. However, we also need to derive conditions on a_{22} and λ . For periodic boundary conditions and requiring a_{22} and $1 - \lambda a_{22}$ to be

positive, we obtain the following estimates

$$\begin{aligned}
 \|w^n\|_\infty &= (1 - \lambda a_{22}) \|w^n\|_\infty + \lambda a_{22} \|w^n\|_\infty = (1 - \lambda a_{22}) \max_j |w_j^n| + \lambda a_{22} \max_j |w_{j-1}^n| \\
 &\geq \max_j \left| (1 - \lambda a_{22}) w_j^n + \lambda a_{22} w_{j-1}^n \right| = \max_j \left| w_j^n - \lambda a_{22} (w_j^n - w_{j-1}^n) \right| \\
 &= \max_j \left| (1 + \mu_\varepsilon a_{22}) w_j^{(2)} - \mu_\varepsilon a_{22} w_{j-1}^{(2)} \right| \geq (1 + \mu_\varepsilon a_{22}) \|w^{(2)}\|_\infty - \mu_\varepsilon a_{22} \|w^{(2)}\|_\infty \\
 &= \|w^{(2)}\|_\infty.
 \end{aligned} \tag{3.10}$$

Further, from $a_{22} > 0$ we immediately obtain a constraint on γ given by $\frac{3\gamma-1}{6\gamma} > 0$, i.e. $\gamma > \frac{1}{3}$ or $\gamma < 0$. Moreover, from $1 - \lambda a_{22} > 0$ we obtain a restriction on the time step given by $\lambda < \frac{6\gamma}{3\gamma-1}$.

Turning to the third stage of the scheme given in (3.5), we obtain

$$\begin{aligned}
 w_j^{(3)} + (1 - \theta_3) c_3 \mu_\varepsilon \Delta_j^{(3)} &= w_j^n - \lambda \left((1 - \theta_3) \tilde{c}_3 \Delta_j^n + \theta_3 \left(\tilde{a}_{31} \Delta_j^{(1)} + \tilde{a}_{32} \Delta_j^{(2)} \right) \right) \\
 &\quad - \mu_\varepsilon \theta_3 \left(a_{32} \Delta_j^{(2)} + a_{33} \Delta_j^{(3)} \right)
 \end{aligned} \tag{3.11}$$

The next step consists in eliminating the terms in $\mu_\varepsilon w^{(2)}$. To that end, we invoke (3.9) to replace $-\mu_\varepsilon \Delta_j^{(2)}$ in (3.11) by

$$-\mu_\varepsilon \Delta_j^{(2)} = \frac{1}{a_{22}} (w_j^{(2)} - w_j^n) + \lambda \Delta_j^n, \tag{3.12}$$

which yields, after some rearranging,

$$\begin{aligned}
 w_j^{(3)} + \mu_\varepsilon \left((1 - \theta_3) c_3 + \theta_3 a_{33} \right) \Delta_j^{(3)} &= w_j^n - \lambda \left((1 - \theta_3) c_3 \Delta_j^n + \theta_3 c_3 \left(\tilde{a}_{31} \Delta_j^n + \tilde{a}_{32} \Delta_j^{(2)} \right) \right) \\
 &\quad + \theta_3 c_3 a_{32} \left(\frac{1}{a_{22}} (w_j^{(2)} - w_j^n) + \lambda \Delta_j^n \right).
 \end{aligned} \tag{3.13}$$

Reformulating (3.13) gives

$$\begin{aligned}
 w_j^{(3)} + \mu_\varepsilon (c_3 + \theta_3 (a_{33} - c_3)) \Delta_j^{(3)} &= \left(1 - \lambda (1 - \theta_3) c_3 - \theta_3 \lambda (\tilde{a}_{31} - a_{32}) - \frac{\theta_3 a_{32}}{a_{22}} \right) w_j^n \\
 &\quad + (\lambda (1 - \theta_3) c_3 + \theta_3 \lambda (\tilde{a}_{31} - a_{32})) w_{j-1}^n \\
 &\quad + \theta_3 \left(\frac{a_{32}}{a_{22}} - \lambda \tilde{a}_{32} \right) w_j^{(2)} + \theta_3 \lambda \tilde{a}_{32} w_{j-1}^{(2)}.
 \end{aligned}$$

To obtain the estimate $\|w^n\|_\infty \geq \|w^{(3)}\|_\infty$, we proceed analogously to the proof for the second stage, given in (3.10). The proof follows the lines of (3.10) and is thus omitted. Like in the second stage, we find that the coefficients in front of w_j and w_{j-1} , at each time level, have to be non-negative. The non-negativity requirements on the coefficients of $w_j^{(2)}$ and $w_{j-1}^{(2)}$ result into the following conditions:

$$\begin{aligned}
 \tilde{a}_{32} \geq 0 &\iff \frac{\gamma(3\gamma^2 + 1)}{3\gamma - 1} \geq 0 \iff \gamma \leq 0 \text{ or } \gamma > \frac{1}{3}, \\
 \frac{a_{32}}{a_{22}} - \lambda \tilde{a}_{32} \geq 0 &\iff \lambda \leq \frac{6\gamma^2}{\gamma(3\gamma^2 + 1)} \text{ and } \gamma > \frac{1}{3}.
 \end{aligned} \tag{3.14}$$

Further, we find, thanks to the coefficient of w_{j-1}^n ,

$$(1 - \theta_3) c_3 + \theta_3 (\tilde{a}_{31} - a_{32}) \geq 0 \iff \theta_3 \frac{3\gamma^2(\gamma + 1)}{3\gamma - 1} \leq \frac{\gamma + 1}{2} \iff \theta_3 \leq \frac{3\gamma - 1}{6\gamma^2}, \tag{3.15}$$

TVD-MOOD SCHEMES

which yields a restriction on θ_3 depending on γ . Another estimate for θ_3 can be obtained from the coefficient of $\Delta_j^{(3)}$:

$$c_3 + \theta_3(a_{33} - c_3) \geq 0 \iff \gamma\theta_3 \leq \frac{\gamma+1}{2} \iff \theta_3 \leq \frac{\gamma+1}{2\gamma}.$$

We see that this condition on θ_3 is less restrictive than the one obtained from (3.15) for all $\gamma > \frac{1}{3}$. Note that $\gamma < 0$ would yield a negative θ_3 , which imposes $\gamma > 0$. The largest value we can take for θ_3 is therefore given by

$$\theta_3^{\text{opt}} = \frac{3\gamma - 1}{6\gamma^2},$$

and θ_3 must satisfy $\theta_3 \leq \theta_3^{\text{opt}}$. Note that the coefficient of w_j^n is always non-negative; indeed,

$$1 - \lambda(1 - \theta_3)c_3 - \theta_3\lambda(\tilde{a}_{31} - a_{32}) - \frac{\theta_3 a_{32}}{c_2} \geq 0, \quad (3.16)$$

is always fulfilled if we set $\theta_3 = \theta_3^{\text{opt}}$. Doing so yields the maximal allowed input from the stages (3.2) of the third order IMEX-RK scheme. Otherwise, (3.16) leads to another, more restrictive estimate for λ .

The final update is given by

$$w_j^{n+1} + (1 - \theta_4)\mu_\varepsilon\Delta_j^{n+1} = w_j^n - \theta_4(\lambda + \mu_\varepsilon)b_2\Delta_j^{(2)} - \theta_4(\lambda + \mu_\varepsilon)b_3\Delta_j^{(3)} - (1 - \theta_4)\lambda\Delta_j^n. \quad (3.17)$$

We again eliminate the terms in $\mu_\varepsilon\Delta_j^{(2)}$ and $\mu_\varepsilon\Delta_j^{(3)}$ in order to avoid a CFL restriction depending on ε . In (3.17), we replace $-\mu_\varepsilon\Delta_j^{(2)}$ by (3.12) and $-\mu_\varepsilon\Delta_j^{(3)}$, using (3.13), by

$$\begin{aligned} -\mu_\varepsilon\Delta_j^{(3)} &= \frac{1}{c_3 + \theta_3(a_{33} - c_3)} \left(w_j^{(3)} - w_j^n \right) + \frac{c_3}{c_3 + \theta_3(a_{33} - c_3)} \lambda \left((1 + \theta_3(\tilde{a}_{31} - 1)) \Delta_j^n + \theta_3\tilde{a}_{32}\Delta_j^{(2)} \right) \\ &\quad - \frac{\theta_3 c_3 a_{32}}{c_3 + \theta_3(a_{33} - c_3)} \left(\frac{1}{a_{22}} (w_j^{(2)} - w_j^n) + \lambda\Delta_j^n \right). \end{aligned}$$

Collecting the terms in front of the states w_j, w_{j-1} at each stage and requiring the positivity of these coefficients gives the L^∞ property $\|w^{n+1}\|_\infty \leq \|w^n\|_\infty$ following analogous steps to (3.10). The resulting requirements on the CFL condition λ and the convex parameter θ_4 are given in Lemma 3.1.

The TVD property can be obtained following the same line of computations as performed for the L^∞ stability and is contained in the following result.

Lemma 3.1 (L^∞ stability, TVD property). *For periodic boundary conditions under the CFL condition*

$$\lambda \leq \frac{18\gamma^3\theta_4 - (3\gamma - 1)(3\gamma^2 + 1)}{(3\gamma - 1)((6\gamma^2 + 1)\theta_4 - (3\gamma^2 + 1))},$$

the scheme consisting of the Butcher tableaux (3.8) with the convex scheme given by the stages (3.6) and the update (3.5) is L^∞ stable and TVD if the following conditions are fulfilled:

$$\gamma \geq \frac{\sqrt{3}}{3}, \quad \theta_1 = 1, \quad \theta_2 = 1, \quad \theta_3 = \frac{3\gamma - 1}{6\gamma^2}, \quad \theta_4 < \frac{(3\gamma - 1)(3\gamma^2 + 1)}{18\gamma^3}. \quad (3.18)$$

3.1.2. TVD conditions for arbitrary number of stages

In the spirit of the results from the second-order scheme, we seek a general framework on how to obtain TVD schemes with s stages using the IMEX formulation (3.6) and (3.5). Since the proof follows analogue steps as in Lemma 3.1, we do not repeat the calculations and we directly give the final result.

Theorem 3.2. *Let $\tilde{A}, A \in \mathbb{R}^{s \times s}$, $\tilde{b}, b, \tilde{c}, c \in \mathbb{R}^s$ define two Butcher tableaux (3.3) fulfilling (3.4) and the p -th order compatibility conditions. Let \tilde{b} and b coincide with the last rows of \tilde{A} and A respectively. For $k = 1, \dots, s$ and $l = 1, \dots, k-1$, we define*

$$\mathcal{A}_k = \theta_k a_{kk} + (1 - \theta_k) c_k, \quad \tilde{\mathcal{A}}_k = \theta_k a_{k1} + (1 - \theta_k) \tilde{c}_k, \quad \mathcal{B}_{kl} = \frac{\theta_k a_{kl}}{\mathcal{A}_l}, \quad \tilde{\mathcal{B}}_{kl} = \theta_k \tilde{a}_{kl}.$$

In addition, we recursively define the following expressions:

$$\begin{aligned} \mathcal{C}_k &= \tilde{\mathcal{A}}_k - \sum_{l=2}^{k-1} \mathcal{B}_{kl} \mathcal{C}_l, & \mathcal{C}_{kl} &= \tilde{\mathcal{B}}_{kl} - \sum_{r=l+1}^{k-1} \mathcal{B}_{kr} \mathcal{C}_{rl}, \\ \mathcal{D}_k &= 1 - \lambda \tilde{\mathcal{A}}_k - \sum_{l=2}^{k-1} \mathcal{B}_{kl} \mathcal{D}_l, & \mathcal{D}_{kl} &= \mathcal{B}_{kl} - \lambda \tilde{\mathcal{B}}_{kl} - \sum_{r=l+1}^{k-1} \mathcal{B}_{kr} \mathcal{D}_{rl}. \end{aligned}$$

Then, with $\theta_1 = 1$ and under the following restrictions for $k = 2, \dots, s$ and $l = 1, \dots, k-1$,

$$\mathcal{A}_k > 0, \quad \mathcal{C}_k \geq 0, \quad \mathcal{D}_k \geq 0, \quad \mathcal{C}_{kl} \geq 0, \quad \mathcal{D}_{kl} \geq 0.$$

the scheme consisting of the stages (3.5) and the update (3.6), combined with a TVD limiter, is L^∞ stable and TVD under a CFL condition determined by $\lambda \geq 0$ where λ does not depend on ε .

We wish to remark that the obtained p -th order tableaux do not necessarily lead to stable schemes by themselves if they are not combined with the convex strategy. This is not a drawback since our goal is the L^∞ stability. For studies on A - or L -stability, we refer to [35].

The result from Theorem 3.2 can be extended to the case where the weights \tilde{b} and b do not coincide with the respective last rows of \tilde{A} and A . To be able to use the notation from Theorem 3.2, we view the update (3.6) as an additional explicit $(s+1)$ -th stage of a scheme induced by Butcher tableaux (3.3) with $(s+1) \times (s+1)$ matrices with the diagonal entry $a_{s+1, s+1} = 0$, where the weights \tilde{b} and b respectively coincide with the last rows of the new \tilde{A} and A . Then we define the convex parameter of the last stage as $\theta_{s+1} = \theta$. Theorem 3.2 is then applied to yield the L^∞ stability and the TVD property. We conclude this section with some remarks.

Remark 3.3. We can prove the same kind of theorem if the first column of A allows for non-zero entries. The TVD conditions obtained when assuming that structure are given in Appendix B.

Remark 3.4. Applying this procedure to a two-stage, second-order scheme, we recover the ARS(2,2,2)-based schemes introduced in [11] and studied more broadly in [33].

3.2. Fully discrete parachute scheme

To increase the resolution of the explicit spatial derivatives, we provide a third-order reconstruction of the cell interface values $w_{j+1/2}$ such that the resulting scheme remains L^∞ stable and TVD. We reconstruct the values $w_j^{(k)}$ using the neighbouring cell averages, see for instance [28]. The reconstructed values $w_{j,-}^{(k)}$ and $w_{j,+}^{(k)}$ at the inner interfaces of cell C_j are then defined by

$$w_{j,-}^{(k)} = w_j^{(k)} - \frac{\Delta x}{2} L \left(\sigma_{j+1/2}^{(k)}, \sigma_{j-1/2}^{(k)} \right), \quad w_{j,+}^{(k)} = w_j^{(k)} + \frac{\Delta x}{2} L \left(\sigma_{j-1/2}^{(k)}, \sigma_{j+1/2}^{(k)} \right), \quad (3.19)$$

where $\sigma_{j+1/2}^{(k)}$ denotes the slope between the values of $w_j^{(k)}$ and $w_{j+1}^{(k)}$ given by

$$\sigma_{j+1/2}^{(k)} = \frac{w_{j+1}^{(k)} - w_j^{(k)}}{\Delta x}.$$

TVD-MOOD SCHEMES

The function $L(\sigma_L, \sigma_R)$ is a slope limiter which should ensure that the reconstructed values still satisfy the maximum principle. For a three-point stencil, the following estimate has to hold

$$\min(|w_{j-1}^{(k)}|, |w_j^{(k)}|, |w_{j+1}^{(k)}|) \leq |w_{j,\pm}^{(k)}| \leq \max(|w_{j-1}^{(k)}|, |w_j^{(k)}|, |w_{j+1}^{(k)}|). \quad (3.20)$$

To increase the space accuracy of the scheme, we use a TVD third-order space reconstruction satisfying (3.20). This merely amounts to setting the limiter function L in the space reconstruction described in (3.19). We choose the third-order limiting procedure introduced in [38]. This procedure switches between the oscillatory non-limited third-order reconstruction and a third-order TVD limiter. Switching to the TVD limiter is triggered in the event where a non-physical oscillation represented by a non-smooth extremum is detected.

In the spirit of the reconstruction used to approximate the explicit derivatives, we could also increase the space accuracy of the implicit derivatives using TVD slope limiters. Note that the slopes are determined in general by a non-linear function. This would mean having to implicitly compute the reconstructed values (3.19). Such computations, if at all doable, would include an iterative process or a prediction correction method and therefore be extremely costly. We consider this increase in computational cost as too much in the sight of the actual gain in resolution.

Another option would be to treat the implicit spacial derivative with a BDF to obtain a high-order approximation. However, this option is unusable here as it would lead to oscillatory solutions, see Appendix A for a proof of this claim. Therefore, we keep the first-order upwind approximation of the implicit spatial derivatives. Note that the IMEX-TVD scheme is overall only of first order. Therefore, this is a loss of resolution in space we are willing to take to obtain a TVD scheme.

Since the third order limiter used on the explicit derivatives is provably TVD according to [38], we apply Theorem 3.2 and immediately find the following result

Corollary 3.5. *The scheme consisting of the Butcher tableaux (3.8), with the stages given in (3.5), the update in (3.6), and combined with the slope limiter from [38], is L^∞ stable and TVD according to Theorem 3.2 with the following choice of parameters*

$$\gamma \geq \frac{\sqrt{3}}{3}, \quad \theta_1 = 1, \quad \theta_2 = 1, \quad \theta_3 = \frac{3\gamma - 1}{6\gamma^2}, \quad \theta_4 < \frac{(3\gamma - 1)(3\gamma^2 + 1)}{18\gamma^3},$$

and under the CFL condition

$$\lambda \leq \frac{18\gamma^3\theta_4 - (3\gamma - 1)(3\gamma^2 + 1)}{(3\gamma - 1)((6\gamma^2 + 1)\theta_4 - (3\gamma^2 + 1))}.$$

An analysis of the influence of the choice of the parameters $\gamma, \theta_3, \theta_4$ and λ is conducted in section 3.3. In particular, the balance between CPU time, i.e. the value of λ , and precision, expressed by the values of θ_3 and θ_4 , is discussed. We emphasise once again that the bound on the time step, expressed by λ , does not depend on ε , which represents the fast scale in equation (2.1).

3.3. Choice of the free parameters

We start these numerical experiments by suggesting optimal values of the free parameters in the TVD scheme of Section 3.1.1, denoted by TVD3. To that end, we analyse the error produced by the schemes, as well as the CPU time taken, with respect to the free parameters. This analysis will help us give some insights on how to optimally choose these parameters, and on the trade-offs that must be made when making such choices.

We compare the IMEX1 scheme to the IMEX3, TVD3 and MOOD3 schemes. Here, the IMEX p scheme is the unlimited scheme of order p in space and time. Following this notation, the IMEX1 scheme is given by (2.5) and the IMEX3 scheme corresponds to the Butcher tableaux (3.8), with a third-order unlimited space discretisation from [38] for the explicit part, and the third-order BDF (A.2)

for the implicit part. The MOOD p scheme is obtained in the framework of Algorithm 1, using the IMEX3 scheme as the high-order scheme and the TVD3 scheme as the parachute scheme. For the model linear multi-scale advection equation, the detection criterion consists in taking the L^∞ norm of the solution, and thus we take $\Phi(w) = w$ in Algorithm 1.

Since the scope of this section is to study the effect of the time discretisation on the precision and computational time of our schemes, we temporarily restrict ourselves to a first-order space discretisation. This ensures that only the effects of the time discretisation are monitored.

An exact solution of the toy problem (2.1) is used for the calibration of the free parameters $\gamma, \theta_3, \theta_4$ and λ in the TVD3 scheme. It is given by

$$w^s(t, x) = 1 + \frac{\varepsilon}{2} \left(1 + \sin \left[2\pi\varepsilon \left(x - \left(c_m + \frac{c_a}{\varepsilon} \right) t \right) \right] \right), \quad (3.21)$$

which represents a sine function of amplitude ε , transported with the velocity $c_m + \frac{c_a}{\varepsilon}$. We set $\varepsilon = 0.1$ and we take $N = 400$ cells. The conclusions of the forthcoming developments are unchanged if we consider other values of ε . Indeed, taking a different ε would merely translate the curves without changing their relative positions. This study is concluded with the results of an optimisation procedure leveraging the conditions of Theorem 3.2 in order to build new Butcher tableaux, and their accompanying values of λ and $\theta_k, k = 1, \dots, s$, that yield TVD schemes.

3.3.1. Choice of γ and θ_4 in the TVD3 scheme

For the TVD3 scheme, we have to set the values of θ_3, θ_4 and λ , constrained by Corollary 3.5. Ideally, we would like θ_3, θ_4 and λ to be as large as possible. By inspection, we note that the maximum value of θ_3 is $\theta_3^{\text{opt}} = \frac{3}{8}$, obtained for $\gamma^{\text{opt}} = \frac{2}{3}$. The Butcher tableaux (3.8) then become

$$\text{explicit: } \begin{array}{c|ccc} 0 & 0 & 0 & 0 \\ \hline \frac{1}{4} & \frac{1}{4} & 0 & 0 \\ \frac{5}{6} & -\frac{13}{18} & \frac{14}{9} & 0 \\ \hline & 0 & \frac{4}{7} & \frac{3}{7} \end{array}, \quad \text{implicit: } \begin{array}{c|ccc} 0 & 0 & 0 & 0 \\ \hline \frac{1}{4} & 0 & \frac{1}{4} & 0 \\ \frac{5}{6} & 0 & \frac{2}{3} & \frac{1}{6} \\ \hline & 0 & \frac{4}{7} & \frac{3}{7} \end{array}. \quad (3.22)$$

Taking this value of γ in Corollary 3.5 yields the following bounds:

$$0 < \theta_4 < \frac{7}{16} \quad \text{and} \quad 0 < \lambda < \frac{7 - 16\theta_4}{7 - 11\theta_4}. \quad (3.23)$$

We note that λ is a decreasing function of θ_4 , which implies that we are not able to use both a large θ_4 and a large λ . There is a trade-off between the CFL condition λ (i.e. the CPU time) and the value of θ (i.e. the resolution of the scheme).

Let us quantify this balance between precision and CPU time. To address this issue, let us introduce $\alpha \in (0, 1)$, to rewrite (3.23) as follows:

$$\theta_4 = \frac{7}{16}\alpha \quad \text{and} \quad \lambda = \frac{1 - \alpha}{1 - \frac{11}{16}\alpha}. \quad (3.24)$$

We note that θ_4 increases and λ decreases when α increases.

We now study the influence of α on the TVD3 scheme with $\gamma = \gamma^{\text{opt}} = \frac{2}{3}$. Note that such a study was performed, for the second-order case, in [33].

We first display in Figure 2 the CPU time with respect to α for the four schemes. As expected, since the CFL condition becomes more restrictive, the CPU time increases with α for the TVD3 and the MOOD3 schemes.

TVD-MOOD SCHEMES

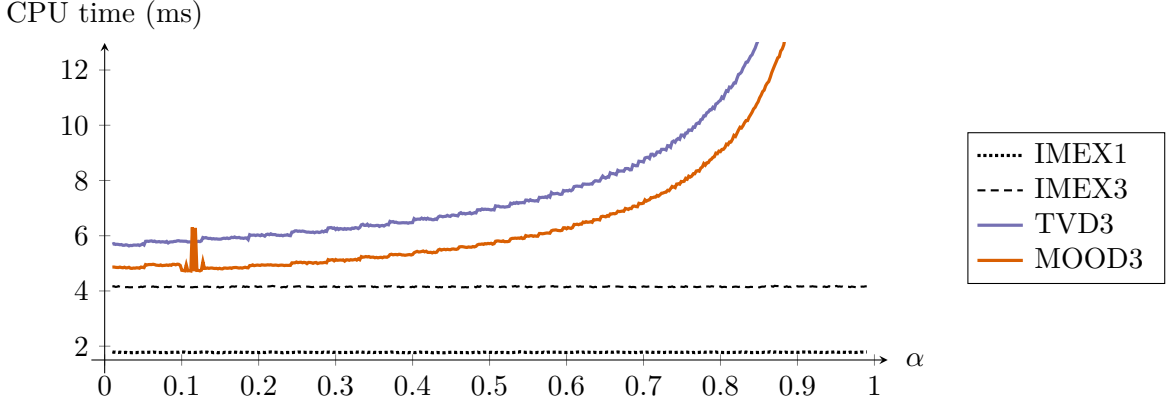


FIGURE 2. CPU time (in milliseconds) with respect to the parameter α , using $\gamma = \gamma^{\text{opt}} = \frac{2}{3}$, in the context of the test case presented in Section 3.3.1.

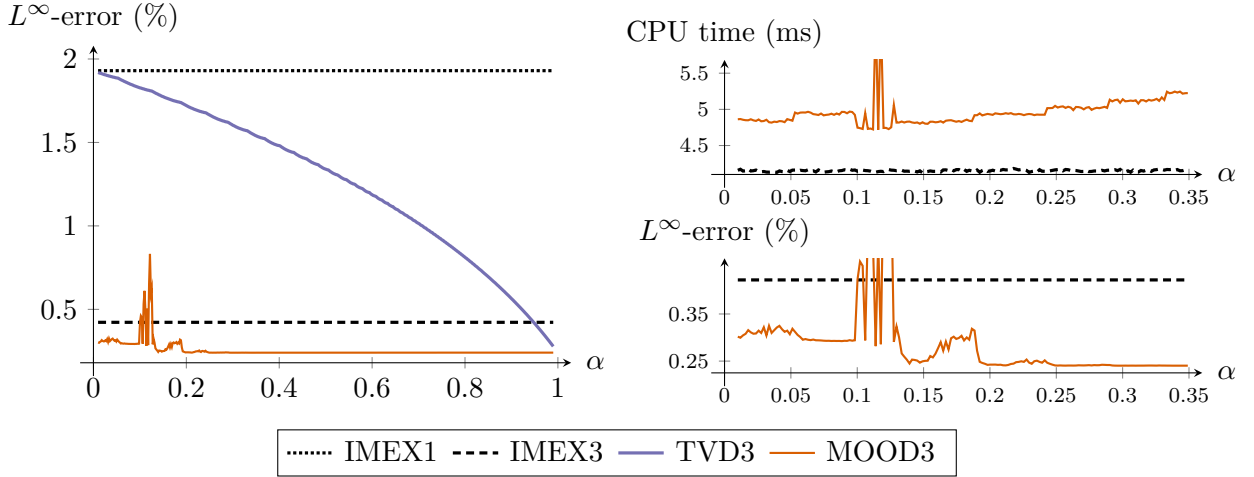


FIGURE 3. L^∞ -error with respect to the parameter α , using $\gamma = \gamma^{\text{opt}} = \frac{2}{3}$, $\theta_3 = \frac{3}{8}$ and θ_4 , λ given by (3.24), in the context of the test case presented in Section 3.3.1. For $\alpha \in (0, 0.35)$, the top right panel contains a zoom on the CPU time (data from Figure 2) and the bottom right panel contains a zoom on the L^∞ -error (data from left panel).

Second, in the left panel of Figure 3, we display the L^∞ -error with respect to α for the four schemes under consideration. As expected, we observe that it decreases with α for the TVD3 scheme, since θ_4 increases.

Third, in the right panel of Figure 3, we display a zoom on the CPU time and the L^∞ -error produced by the IMEX3 and MOOD3 schemes, with respect to $0 < \alpha < 0.35$. We observe that the error stabilizes around $\alpha = 0.3$, and that the CPU time increases monotonically with α .

Therefore, taking $\alpha = \frac{1}{3}$ seems to be a good compromise between precision and computational time. In the remainder of this article, we take

$$\gamma = \gamma^{\text{opt}} = \frac{2}{3} \quad \text{and} \quad \alpha = \alpha^{\text{opt}} = \frac{1}{3},$$

which leads to the following values for θ_3 , θ_4 and λ :

$$\theta_3^{\text{opt}} = \frac{3}{8} = 0.375, \quad \theta_4^{\text{opt}} = \frac{7}{48} \simeq 0.146, \quad \text{and} \quad \lambda^{\text{opt}} = \frac{32}{37} \simeq 0.865.$$

3.3.2. Numerical optimisation of larger Butcher tableaux

To conclude this Section, we mention two other Butcher tableaux that yield a TVD scheme. To obtain these tableaux, we have used the TVD inequalities from Theorem 3.2, as well as the order conditions as constraints in an optimisation problem where the objective is to maximize the value of $\lambda + \sum \theta$, and where the unknowns are the Butcher coefficients, the values of θ and λ . We ran this optimization problem with many random initial conditions for the unknowns, and we refined this random initialisation around values yielding a large value of the objective function. In the end, we chose the solution where the value of the objective function was maximal, under the additional constraint that $\lambda \geq 0.5$ which is a standard CFL condition arising in fluid dynamics schemes.

For a four-step third-order tableau, we obtain $\lambda = 0.5471076190680170$, $\theta_1 = 1$, $\theta_2 = 1$, $\theta_3 = 1$, $\theta_4 = 0.5110907014643069$ and $\theta_5 = 0.4997722865197203$. The Butcher tableaux are given in Appendix C. In the remainder of the paper, the scheme and its MOOD version will be referred to as TVD3(4) and MOOD3(4).

4. Numerical results

In this last section, we illustrate the capabilities of the schemes we have developed in the previous sections. We first apply the TVD-MOOD strategy to the toy problem in section 4.1, before moving on to the 2D isentropic Euler system in section 4.2.

4.1. Linear multi-scale advection equation

In this section, we consider several numerical experiments, with some common characteristics. In each experiment, we prescribe periodic boundary conditions, and we take $c_m = 1$ and $c_a = 1$. The value of the fast transport velocity therefore is $1/\varepsilon$. The values of ε will vary throughout the experiments to highlight how the results depend on ε . The space-time domain is taken such that the solution revolves exactly once with the periodic boundary conditions, i.e. we take the final time $t_{\text{end}} = 1$ and space domain $(0, c_m + \frac{c_a}{\varepsilon})$.

We introduce a discontinuous exact solution to the initial value problem (2.1), which will help us demonstrate the properties of the schemes. This discontinuous solution $w^d(t, x)$ is given by

$$w^d(t, x) = \begin{cases} 1 + \varepsilon & \text{if } \frac{1}{4} < \left(\frac{(x - (c_m + \frac{c_a}{\varepsilon})t)}{c_m + \frac{c_a}{\varepsilon}} - \left\lfloor \frac{(x - (c_m + \frac{c_a}{\varepsilon})t)}{c_m + \frac{c_a}{\varepsilon}} \right\rfloor \right) < \frac{3}{4} \\ 1 & \text{otherwise,} \end{cases} \quad (4.1)$$

which represents a rectangular bump of amplitude ε , transported with the velocity $c_m + \frac{c_a}{\varepsilon}$, and initially located in the space region $(\frac{1}{4}(c_m + \frac{c_a}{\varepsilon}), \frac{3}{4}(c_m + \frac{c_a}{\varepsilon}))$. This exact solution will be taken as initial data by setting $t = 0$. The detection criterion, like in section 3.3.1, is the L^∞ norm of the solution:

$$\Phi(w) = w. \quad (4.2)$$

We first use this simple multi-scale advection case to demonstrate a few properties of the TVD-MOOD approach. In section 4.1.1, we highlight the flexibility of such approaches, as well as the important gain in space-time error obtained by using good parachute schemes. Then, in section 4.1.2, we study the approximation of a discontinuous solution in more detail. In particular, we show that the loss of convergence due to overshoots and undershoots is compensated by our approach.

TVD-MOOD SCHEMES

Remark 4.1. In the following numerical experiments, some values of the number of points N are large when ε is small. These large values of N have been chosen to ensure that more than 10 time iterations are needed to reach t_{end} . If fewer time iterations are considered, the time steps are too large to visually notice the differences between the schemes.

4.1.1. Perks of the TVD-MOOD approach

We start the numerical experiments by showing a few important perks of the TVD-MOOD strategy. We first show the flexibility of our large time step schemes compared to L -stable and SSP IMEX schemes from the literature. Then, we exhibit the main advantage of the first-order schemes developed in this paper: even though they are first-order accurate, their errors are smaller than the ones of the classical first-order schemes, which results in an overall better space-time error.

To provide a point of comparison with the schemes derived in this paper, we introduce the L -stable ARS(2,3,3) scheme, reported in [3], Section 2.4, or [35], Table 5. It is given by the following tableaux

$$\text{expl.: } \begin{array}{c|ccc} 0 & 0 & 0 & 0 \\ \delta & \delta & 0 & 0 \\ \hline 1-\delta & \delta-1 & 2-2\delta & 0 \\ \hline & 0 & 1/2 & 1/2 \end{array}, \quad \text{impl.: } \begin{array}{c|ccc} 0 & 0 & 0 & 0 \\ \delta & 0 & \delta & 0 \\ \hline 1-\delta & 0 & 1-2\delta & \delta \\ \hline & 0 & 1/2 & 1/2 \end{array}, \quad \text{where } \delta = \frac{3+\sqrt{3}}{6}.$$

Note that this scheme falls within the framework of section 3.1.1. Indeed, the above tableaux are nothing but the tableaux (3.8) with $\gamma = \frac{3-\sqrt{3}}{6}$. This value of γ does not satisfy the requirement of Corollary 3.5, and therefore we cannot prove the existence of convex combinations that make the ARS(2,3,3) scheme TVD and L^∞ stable with a CFL restriction independent of ε . The following numerical experiments should therefore highlight that the property of L -stability is not enough to ensure non-oscillatory approximations.

Flexibility of large time step schemes. We are concerned with a comparison of the MOOD3(4) with schemes from the literature. Namely, we consider the aforementioned ARS(2,3,3) scheme from [3], as well as a more recent SSP-IMEX scheme from [9], Section 3.2.3, which we label as CGGS3. To compare the results of these two schemes with our MOOD3(4) scheme, we choose to compute both the CPU time and the L^1 error, for the discontinuous solution (4.1) with $N = 4000$ and $\varepsilon = 10^{-3}$.

By inspection, we remark that for the ARS(2,3,3) and CGGS3 schemes to be L^∞ stable, the ε -dependent CFL restriction $\lambda \leq 0.9\varepsilon$ is required, while for the MOOD3(4) scheme it is enough to take $\lambda < \lambda^{\text{opt}} \simeq 0.547$.

The results are displayed in Table 1. We observe that the errors and CPU times of the ARS(2,3,3) and CGGS3 schemes are similar for $\lambda = 0.9\varepsilon$. However, in the case of the MOOD3(4) scheme, we can take a much larger range of λ . Indeed, by taking a larger λ , we can choose to sacrifice accuracy and gain CPU time, as evidenced by the first lines of Table 1. Then, taking a smaller λ , for instance $\lambda = 2\varepsilon$, yields a similar CPU time and error compared to the ARS(2,3,3) and CGGS3 schemes.

This series of numerical experiments highlights the flexibility of our approach. Based on the desired application and focus where L^∞ stability is required, thanks to large time step schemes, one may choose either a fine resolution following the fastest scale when necessary at the cost of a larger CPU time, or a smaller CPU time when a coarser resolution is sufficient in the numerical result. We want to stress that one is limited to the fine resolution and a large CPU time if considering schemes such as ARS(2,3,3) or CGGS3.

Space-time error of the TVD-MOOD approach. We now address the advantage of using the schemes that have been derived in this paper as parachute schemes, as opposed to using the classical

TABLE 1. CPU times and L^1 errors for discontinuous solution (4.1) with $N = 4000$ discretisation points and $\varepsilon = 10^{-3}$, using the MOOD3(4), ARS(2,3,3) and CGGS3 schemes.

	λ	CPU time (s)	L^1 error
MOOD3(4)	$\lambda = \lambda^{\text{opt}} \simeq 0.548$	0.0101	0.217
	$\lambda = 250\varepsilon = 0.25$	0.0222	0.111
	$\lambda = 50\varepsilon = 0.05$	0.0953	0.0591
	$\lambda = 10\varepsilon = 0.01$	0.659	0.0488
	$\lambda = 2\varepsilon = 0.0002$	1.63	0.0253
	$\lambda = 0.9\varepsilon = 0.0009$	3.64	0.0253
CGGS3	$\lambda = 0.9\varepsilon = 0.0009$	1.25	0.0253
ARS(2,3,3)	$\lambda = 0.9\varepsilon = 0.0009$	1.17	0.0253

first-order IMEX schemes. Recall that the class of schemes derived in Section 3 consists in first-order schemes. However, an important point to quantify is the gain in error made by using our new schemes as parachute schemes. Since the TVD p schemes have a higher resolution than the IMEX1 scheme, we expect the MOOD procedure to yield an approximation that is consistently better over time. Indeed, if there is an oscillation at some time t^n , then the solution at time t^{n+1} approximated by the IMEX1 scheme will be significantly more diffused than the one yielded by the TVD p scheme. Hence, over time, the approximate solution should be, on average, farther from the exact solution when using the IMEX1 scheme as a parachute rather than the TVD p scheme. To quantify this intuition, let us introduce the following space-time errors, which measure the average and maximum errors, caused by diffusion, between the solution and the exact solution:

$$e_{\text{ST}}^{\text{mean}} = \frac{1}{n_t} \sum_{n=1}^{n_t} \left[\left(\max_j (w_{\text{ex}})_j^n - \min_j (w_{\text{ex}})_j^n \right) - \left(\max_j w_j^n - \min_j w_j^n \right) \right],$$

$$e_{\text{ST}}^{\text{max}} = \max_{1 \leq n \leq n_t} \left[\left(\max_j (w_{\text{ex}})_j^n - \min_j (w_{\text{ex}})_j^n \right) - \left(\max_j w_j^n - \min_j w_j^n \right) \right],$$

where n_t is the number of time iterations.

In Table 2, we report the values of $e_{\text{ST}}^{\text{mean}}$ and $e_{\text{ST}}^{\text{max}}$ with respect to $\varepsilon \in \{1, 10^{-1}, 10^{-2}, 10^{-3}\}$. The errors are obtained when approximating the discontinuous solution (4.1) with $25/\varepsilon$ cells. We note that, for the mean and maximum space-time errors, using the TVD3(4) scheme as a parachute lowers the error by a factor of up to 3 for small values of ε . Since small values of ε represent the most likely use case of the TVD-MOOD approach, this represents a strong argument in favour of our technique.

4.1.2. Approximation of a discontinuous solution

Now, we study the numerical approximation of the discontinuous solution (4.1) with the IMEX3, TVD3, MOOD3 and MOOD3(4) schemes.

Here, to compute the order of accuracy of the scheme, we no longer focus on the L^∞ norm, which is not suited to the computation of an error between a discontinuous solution and its diffusive approximation. Instead, we turn to the L^1 norm, defined by

$$\|w^n\|_1 = \frac{1}{\Delta x} \sum_j |w_j^n|.$$

However, the above norm only measures the average deviation between the exact solution and the numerical approximation. Here, since we seek a measure of the maximum principle violation of the

TVD-MOOD SCHEMES

TABLE 2. Space-time error with respect to ε . The results of the TVD-MOOD approach (using the TVD3(4) scheme as a parachute scheme) are compared to the results of using the classical IMEX1 scheme as a parachute scheme. The space-time error is lower by a factor of about 3 for low values of ε when using the newly derived schemes as parachutes for the MOOD method.

	mean spacetime error			maximum spacetime error		
	☯: IMEX1	☯: TVD3(4)	ratio	☯: IMEX1	☯: TVD3(4)	ratio
$\varepsilon = 1$	1.23×10^{-2}	8.92×10^{-3}	1.37	2.25×10^{-2}	1.98×10^{-3}	1.13
$\varepsilon = 10^{-1}$	5.57×10^{-5}	2.56×10^{-5}	2.17	1.67×10^{-4}	7.99×10^{-5}	2.10
$\varepsilon = 10^{-2}$	2.72×10^{-4}	9.22×10^{-5}	2.95	1.34×10^{-3}	5.77×10^{-4}	2.33
$\varepsilon = 10^{-3}$	2.82×10^{-4}	9.69×10^{-5}	2.91	1.68×10^{-3}	5.92×10^{-4}	2.84

IMEX $_p$ scheme, we instead consider the following modification of the L^1 norm:

$$\|w^n\|_{L^1_0} = \frac{1}{\Delta x} \sum_j \left(|w_j^n| + \max_{m \leq n} \left[\left(\max_j w_j^m - \min_j w_j^m \right) - \left(\max_j w_j^0 - \min_j w_j^0 \right) \right] \right).$$

This quantity, although it does not satisfy the triangle inequality property of a norm, as it is in fact a quasinorm, allows us to add the impact of overshoots and undershoots to the usual measure of the average deviation between the solution and its approximation. Since the TVD $_p$ and MOOD $_p$ methods are built to avoid such over- and undershoots, this additional term will vanish with these methods.

We turn to Figure 4, where we have displayed the numerical approximation of the discontinuous solution by the IMEX1, ARS(2,3,3), IMEX3, TVD3, MOOD3 and MOOD3(4) schemes, for $\varepsilon = 1$ in the left panel and $\varepsilon = 10^{-3}$ in the right panel. As usual, we note that the pure IMEX high-order schemes are oscillatory and violate the maximum principle, while the other four schemes are in-bounds. A notable remark concerns the IMEX3 scheme when $\varepsilon = 10^{-3}$, in the right panel depicted by the dashed line. In this case, the scheme is so unstable that the numerical solution is unrecognisable. The MOOD3 scheme corrects this shortcoming. Furthermore, the MOOD3(4) scheme is based on a more stable third-order scheme, which ensures a better approximation of the exact solution.

In Figure 5, we report the error produced by the six schemes, in the L^1 norm in the left panels and in the L^1_0 quasinorm in the right panels, for $\varepsilon = 1$ in the top panels and $\varepsilon = 10^{-3}$, except for the IMEX3 scheme, whose error would explode in the bottom panels. First, we observe that the theoretical order of convergence is not reached. We get an accuracy up to order $\frac{1}{2}$ for the IMEX1, TVD3, MOOD3 and MOOD3(4) schemes, and up to order $\frac{3}{4}$ for the ARS(2,3,3) and IMEX3 schemes. This is due to the fact that we approximate a discontinuous solution, where the numerical diffusion of the schemes considerably worsen the order of convergence, see for instance [28], Chapter 11. Second, the L^1 -error of the ARS(2,3,3) scheme is lower than the one of the other schemes (except for the MOOD3(4) scheme). However, when taking the over- and undershoots into account thanks to the L^1_0 quasinorm, we observe that the L^1_0 quasinorm of the error produced by the IMEX1, TVD3, MOOD3 and MOOD3(4) schemes is the same as their L^1 norm. This was to be expected since no over- or undershoots are produced by these schemes. However, when looking at the L^1_0 quasinorm of the error of the ARS(2,3,3) scheme, we observe that it stays roughly constant as N grows larger. This means that the improvement in L^1 norm, since the numerical solution is overall closer to the exact solution, is almost exactly compensated by an increase of the over- and undershoot magnitude. Therefore, even taking large N is not enough to ensure a good approximation of the exact discontinuous solution by the ARS(2,3,3) scheme.

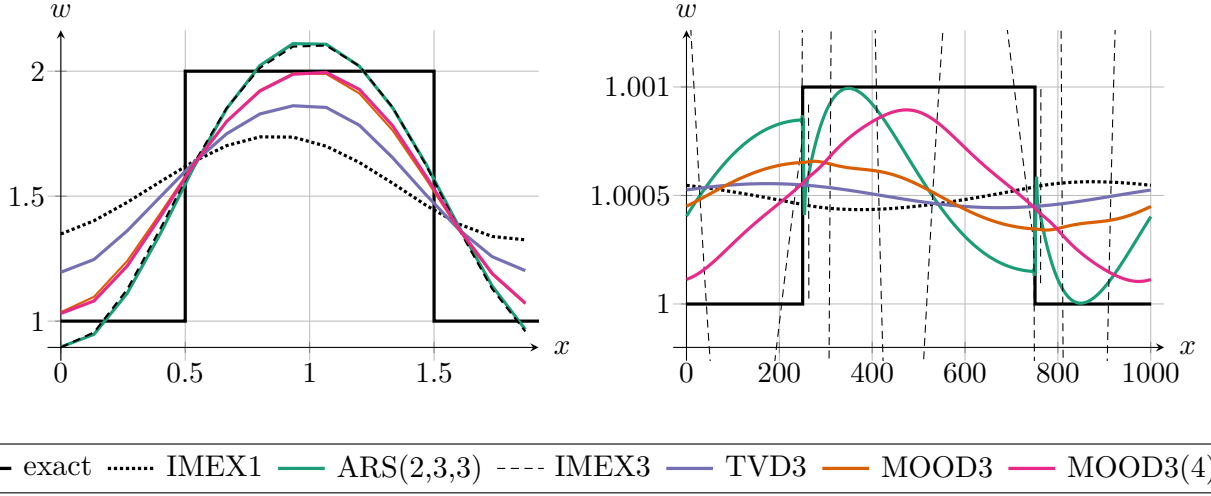


FIGURE 4. Approximation of the discontinuous solution (4.1) at time t_{end} using the IMEX1, ARS(2,3,3), IMEX3, TVD3 and MOOD3 schemes. Left panel: $\varepsilon = 1$ and $\Delta x \simeq 0.13$; right panel: $\varepsilon = 10^{-3}$ and $\Delta x \simeq 0.67$. In the right panel, the errors produced by the IMEX3 scheme have destroyed the numerical approximation.

4.2. Application to the isentropic Euler equations

In these last numerical experiments, we consider an application of the TVD-MOOD strategy to the isentropic Euler equations. This system models fluid flows. It is governed, in one space dimension and after a suitable rescaling, by:

$$\begin{cases} \partial_t \rho + \nabla \cdot (\rho \mathbf{u}) = 0, \\ \partial_t (\rho \mathbf{u}) + \nabla \cdot (\rho \mathbf{u} \otimes \mathbf{u}) + \frac{1}{M^2} \nabla p(\rho) = \mathbf{0}, \end{cases} \quad (4.3)$$

where $\rho(x, t) > 0$ is the fluid density and $\mathbf{u}(x, t) = (u(x, t), v(x, t))$ is its velocity. Assuming an ideal gas, the pressure is $p(\rho) = \rho^\gamma$, with $\gamma \geq 1$ the ratio of specific heats. Finally, M is the Mach number, which represents the ratio of material to acoustic velocity. The system (4.3) describes a compressible flow for $M > 0$, whereas the flow becomes incompressible when M tends to 0. For more information, see for instance [26, 30].

We are specifically concerned with schemes that behave correctly in the low Mach number limit. Such schemes have been the focus of much work in the recent past, see for instance [10, 12, 5], but this list is far from being exhaustive. In this section, we focus on the scheme derived in [12], whose semi-discretization in time reads:

$$\begin{cases} \frac{\rho^{n+1} - \rho^n}{\Delta t} + \nabla \cdot (\rho \mathbf{u})^{n+1} = 0, & (4.4c) \\ \frac{(\rho \mathbf{u})^{n+1} - (\rho \mathbf{u})^n}{\Delta t} + \nabla \cdot (\rho \mathbf{u} \otimes \mathbf{u})^n + \frac{1}{M^2} \nabla p(\rho^{n+1}) = \mathbf{0}. & (4.4d) \end{cases}$$

We recast (4.4) under the following condensed form:

$$\frac{W^{n+1} - W^n}{\Delta t} + \nabla \cdot \mathbf{F}_e(W^n) + \nabla \cdot \mathbf{F}_i(W^{n+1}) = 0, \quad (4.5)$$

TVD-MOOD SCHEMES

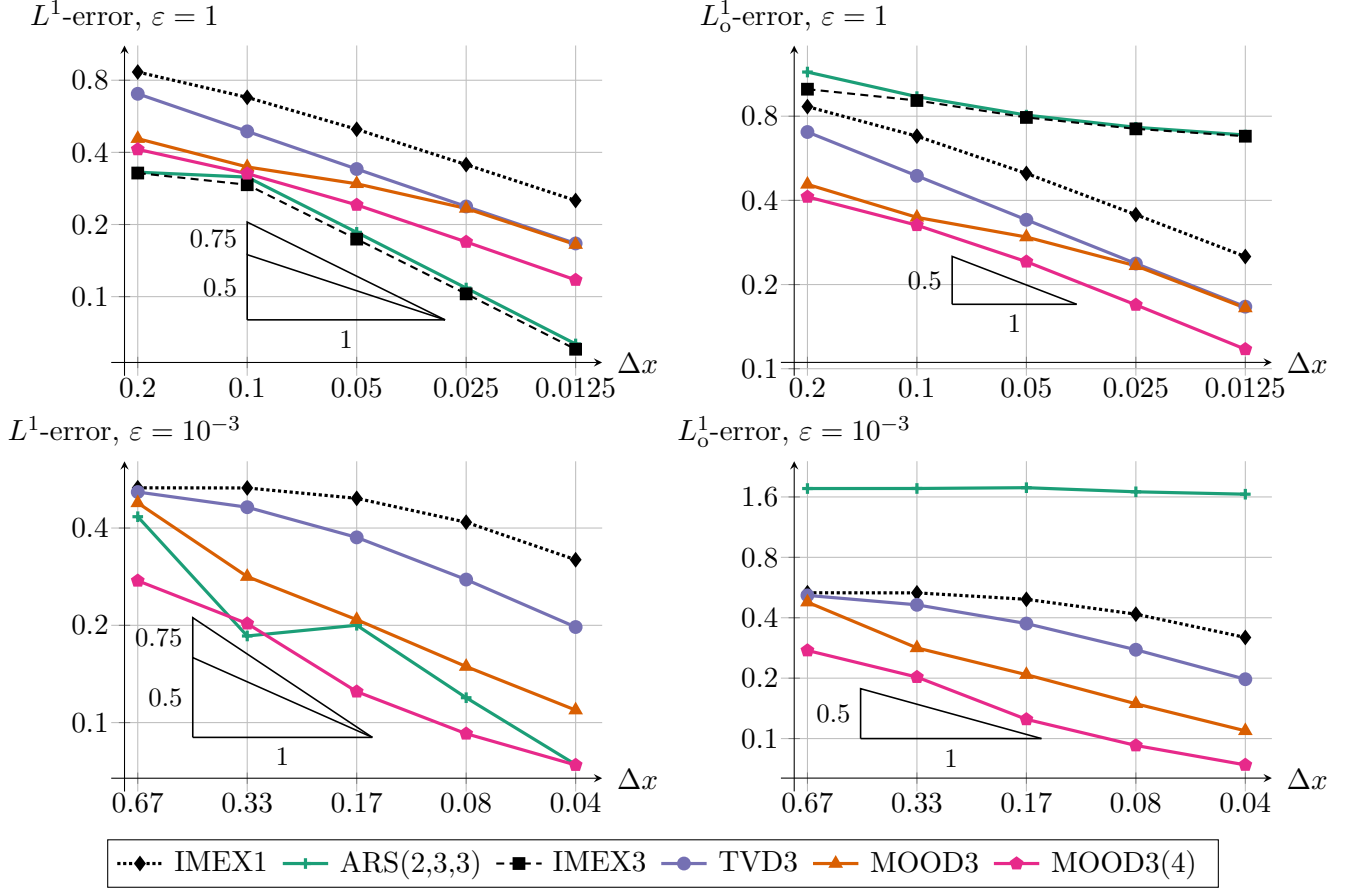


FIGURE 5. Error lines in L^1 norm (left panels) and L^1_0 quasinorm (right panels) for the discontinuous solution (4.1) using the IMEX1, ARS(2,3,3), IMEX3, TVD3, MOOD3 and MOOD3(4) schemes. Top panels: $\varepsilon = 1$; bottom panels: $\varepsilon = 10^{-3}$. For $\varepsilon = 10^{-3}$, the IMEX3 error is so large that the error lines are not displayed (see Figure 4, right panel).

where we have set

$$W = \begin{pmatrix} \rho \\ \rho u \\ \rho v \end{pmatrix}; \quad \mathbf{F}_e(W) = \begin{pmatrix} 0 & 0 \\ \rho u^2 & \rho uv \\ \rho uv & \rho v^2 \end{pmatrix}; \quad \mathbf{F}_i(W) = \begin{pmatrix} \rho u & \rho v \\ \frac{1}{M^2} p(\rho) & 0 \\ 0 & \frac{1}{M^2} p(\rho) \end{pmatrix}, \quad (4.6)$$

with F_e and F_i respectively being the explicit and implicit fluxes. Note that the seemingly coupled system (4.4) can be decoupled by inserting the value of $(\rho \mathbf{u})^{n+1}$ from (4.4d) into (4.4c).

There is a natural correspondence between the Euler equations (4.5) and the toy problem (2.1). Indeed, $\mathbf{F}_e(W)$ corresponds to $c_m w$ and $\mathbf{F}_i(W)$ corresponds to $\frac{c_a}{\varepsilon} w$, with ε representing the square Mach number M^2 . Therefore, once a suitable space discretisation is chosen for (4.5), applying the IMEX p and TVD p schemes is straightforward in the finite volume framework. For the TVD p scheme, the same value of θ that was derived for the toy problem is directly used for the Euler system. In addition, the high-order extension in space consists in a polynomial reconstruction procedure as well as some modifications in the computation of the flux. For example, this framework is discussed in [8] for

unstructured meshes and detailed in [32] for Cartesian grids. However, adapting the MOOD p scheme requires the introduction of a new detection criterion.

Indeed, since the Euler equations (4.3) form a hyperbolic system of conservation laws, the basic MOOD criterion (4.2) on the L^∞ norm of the unknown w , that was used for the linear multi-scale advection equation, is no longer valid. Instead, we follow [11] and use the Riemann invariants to detect oscillations, since we know from [40] that at least one of the Riemann invariants satisfies a maximum principle in a 1D Riemann problem. To adapt this to our 2D Cartesian framework, we use the normal velocity to define the Riemann invariants at each edge of the mesh:

$$\Phi_\pm(W) = \mathbf{u} \cdot \mathbf{n} \mp \frac{1}{M} \frac{2}{\gamma - 1} \sqrt{\gamma \rho^{\gamma-1}},$$

where \mathbf{n} is the outward unit vector normal to the edge. They are thus used as a time-dependent detection criterion in Algorithm 1, by taking $\Phi = \max(\Phi_-, \Phi_+)$.

Regarding the space discretisation, we focus on the finite volume scheme proposed in [12], which has been built to ensure the L^∞ stability on a linearized version of (4.3), at the cost of some extra numerical viscosity, proportional to $1/M$, in the implicit flux. For the sake of conciseness, we do not rewrite this space discretisation here; the reader is referred to [12, 11] for more information.

Remark 4.2. We introduce an important difference with respect to the strategy from [11]. Indeed, in [11], the unlimited second-order scheme was nothing but a straightforward extension of the first-order scheme. Therefore, there remained a viscosity term in $1/M$ in the unlimited second-order scheme. In the following experiments, the unlimited third-order scheme has a vanishing implicit viscosity term. This allows the unlimited scheme to be asymptotic-preserving in space, contrary to the scheme from [11]. The parachute scheme remains the TVD scheme with a large implicit viscosity, to ensure that the TVD-MOOD strategy indeed devolves into a TVD scheme when the stability criteria are violated.

This space-time discretisation allows us to take a time step constrained by

$$\Delta t \leq C \frac{\delta}{2 \max(\max_j |u_j|, \max_j |v_j|)}, \quad (4.7)$$

which does not depend on the Mach number M , unlike in the case of classical explicit schemes. In (4.7), δ represents the mesh step. For the uniform Cartesian grids used in the numerical experiments, we take $\delta = \min(\Delta x, \Delta y)$.

Equipped with the TVD-MOOD strategy for the 2D isentropic Euler equations, we now apply it on Cartesian grids. First, we test the TVD property on a discontinuous solution, namely a Riemann problem, in section 4.2.1. Then, we approximate a shear wave in section 4.2.2, and we finally show the order of accuracy of the TVD-MOOD method on a smooth vortex in section 4.2.3. Motivated by the results of the previous section, which are only exacerbated in the Euler case, and for the sake of clarity, we do not present the results of the TVD3, IMEX3 and MOOD3 schemes. Instead, we only display the results of the IMEX1 and MOOD3(4) schemes. Indeed, in all cases where the Mach number was small, the IMEX3 scheme and the other unlimited time discretisations were not exploitable.

4.2.1. Approximation of a Riemann problem

We first apply the schemes to the approximation of a discontinuous solution. In this context of the isentropic Euler equations, we propose a simulation of the following Riemann problem with well-prepared initial data:

$$\begin{cases} \rho(x, y, 0) = \begin{cases} 1 + M^2 & \text{if } x < 1, \\ 1 & \text{otherwise,} \end{cases} \\ (\rho u)(x, y, 0) = 0, \\ (\rho v)(x, y, 0) = 0. \end{cases} \quad (4.8)$$

TVD-MOOD SCHEMES

Note that this initialisation mimics a one-dimensional Riemann problem in the x -direction. We take $\gamma = 1.4$ and we compute the solution until the final time $t_{\text{end}} = 0.3M$ on the space domain $(0, 2) \times (0, 1)$, equipped with Neumann boundary conditions. Also, to eliminate more oscillations, we take $\xi = \frac{1}{100}$. Note that this problem is fundamentally one-dimensional. Therefore, we consider a mesh with N cells in the x -direction and 3 cells in the y -direction. The approximations are depicted in Figures 6 and 7 for, respectively, $M = 1$ with $N = 50$, and $M = 10^{-2}$ with $N = 2500$.

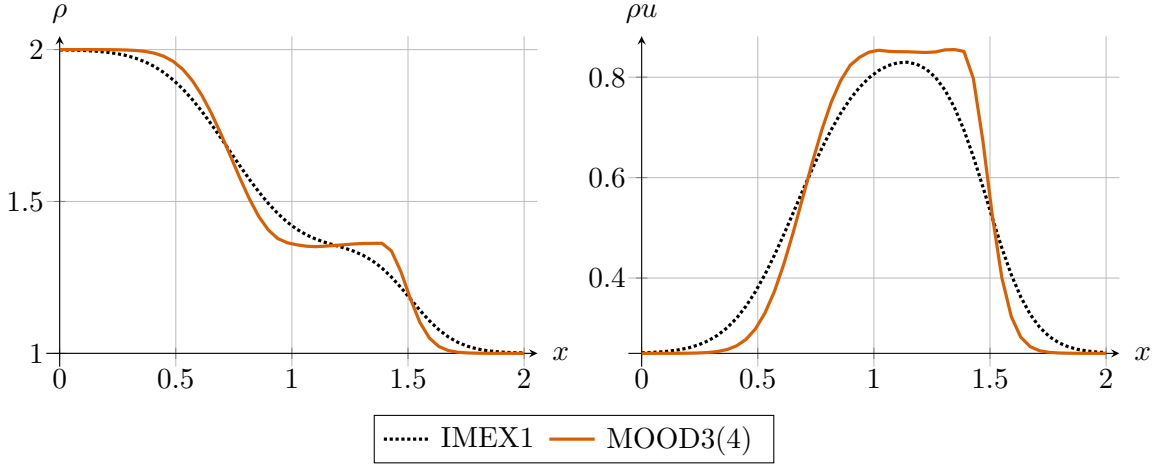


FIGURE 6. Approximation of the solution to the Riemann problem (4.8) at time t_{end} with $M = 1$, on a 50×3 mesh, and using the IMEX1 and MOOD3(4) schemes. Left panel: density ρ ; right panel: momentum ρu .

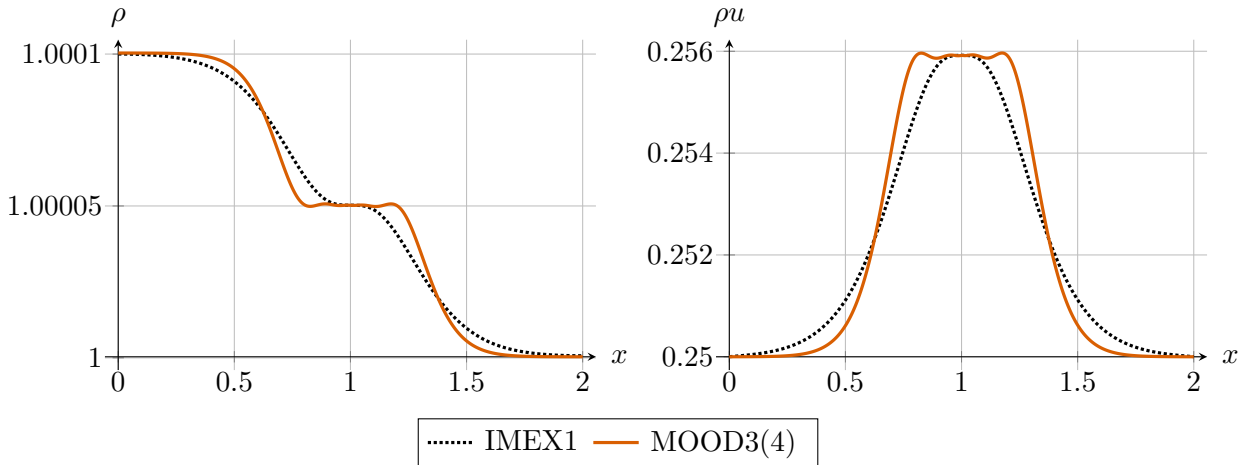


FIGURE 7. Approximation of the solution to the Riemann problem (4.8) at time t_{end} with $M = 10^{-2}$, on a 2500×3 mesh, and using the IMEX1 and MOOD3(4) schemes. Left panel: density ρ ; right panel: momentum ρu .

Similar conclusions as in Section 4.1.2 are drawn from this experiment. For $M = 1$ and $M = 10^{-2}$, the MOOD procedure is activated respectively 62% and 50% of time iterations. This observation is explained by the fact that the IMEX3(4) scheme is quite oscillatory, and its oscillations have to be

countered by the MOOD procedure. The share of iterations where the MOOD procedure was activated could be lowered by basing the MOOD procedure on a less oscillatory third-order IMEX scheme than the IMEX3(4) scheme.

Furthermore, as expected, these schemes allow us to use a time step much larger than classical explicit schemes when the Mach number is low. Indeed, for $M = 1$, we get a time step of the same order as the classical one, whereas in the low Mach number regime where $M = 10^{-2}$, we can use the time step $\Delta t \simeq 1.9 \times 10^{-4}$, which is about $10^2 = \frac{1}{M}$ times larger than the classical explicit scheme with $\Delta t \simeq 8.3 \times 10^{-7}$.

4.2.2. Shear wave

We now turn to the approximation of a shear wave. The well-prepared initial data are given by:

$$\begin{cases} \rho(x, y, 0) = \begin{cases} 1 + M^2 & \text{if } x < 1, \\ 1 & \text{otherwise,} \end{cases} \\ (\rho u)(x, y, 0) = 0, \\ (\rho v)(x, y, 0) = \begin{cases} 1 + M & \text{if } x < 1, \\ 1 & \text{otherwise.} \end{cases} \end{cases} \quad (4.9)$$

Such data produce a single shear wave, i.e. a contact discontinuity in the y -velocity, which travels at a slower velocity than the acoustic waves. This experiment is designed to highlight our scheme's ability to maintain reasonable accuracy in the approximation of the acoustic waves, while still providing a sharp approximation of the shear wave. Having such properties is important in the simulation of some real-world events, such as vapour explosions [20]. We still consider a $N \times 3$ mesh to account for the one-dimensionality of the problem.

We take $\gamma = 1.4$ and the solution is computed until the final time $t_{\text{end}} = 0.25M$ on the space domain $(0, 2) \times (0, 1)$, equipped with Neumann boundary conditions. We take $\xi = \frac{1}{100}$. The approximations are depicted in Figures 8 and 9 for, respectively, $M = 1$ with $N = 50$, and $M = 10^{-2}$ with $N = 1000$.

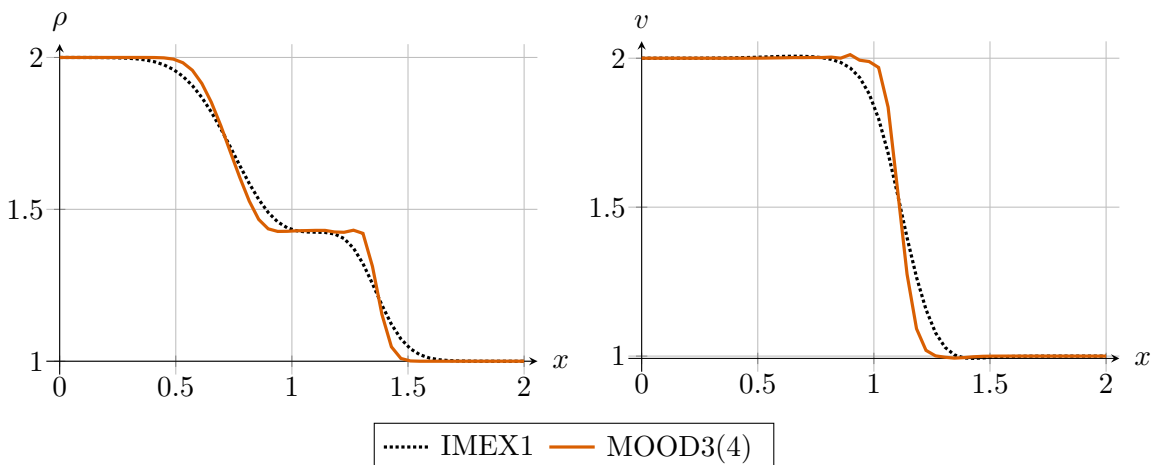


FIGURE 8. Shear wave experiment: approximation of the solution to the Riemann problem (4.9) at time t_{end} with $M = 1$, on a 50×3 mesh, using the IMEX1 and MOOD3(4) schemes. Left panel: density ρ ; right panel: y -velocity v .

TVD-MOOD SCHEMES

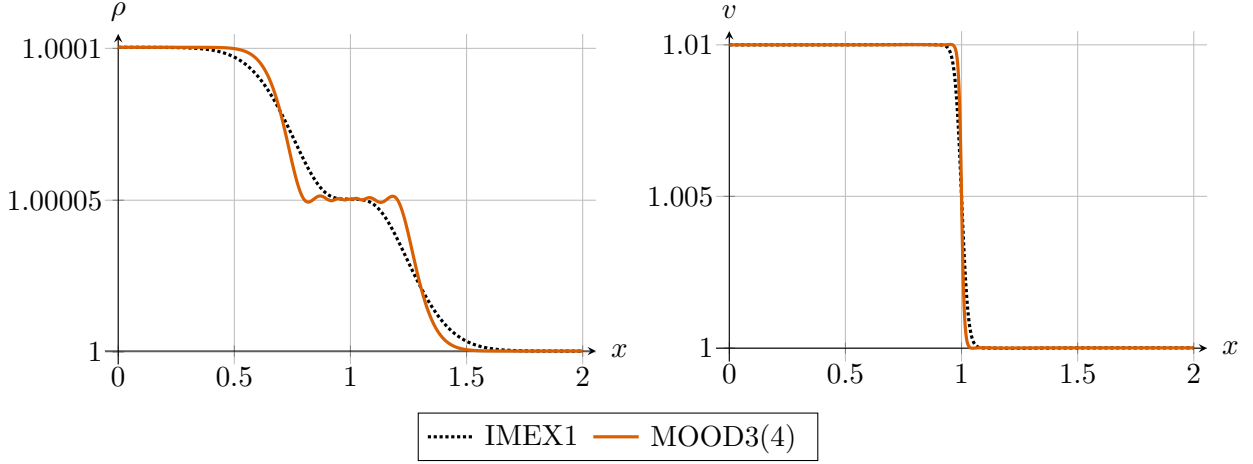


FIGURE 9. Shear wave experiment: approximation of the solution to the Riemann problem (4.9) at time t_{end} , with $M = 10^{-2}$, on a 1000×3 mesh, using the IMEX1 and MOOD3(4) schemes. Left panel: density ρ ; right panel: y -velocity v .

We observe, as expected, that the approximation of the shear wave is quite sharp, and that the acoustic waves are not diffused away as is common in usual approaches. This time, for $M = 1$ and $M = 10^{-2}$, the MOOD procedure is activated respectively 53% and 40% of time iterations.

4.2.3. Bidimensional vortex

We consider the following exact solution of the 2D Euler equations:

$$\begin{cases} \rho(x, y) = 1 - \frac{M^2}{8} e^{-2a^2 r(x, y)^2}, \\ u(x, y) = ay \sqrt{\frac{\gamma}{2}} e^{-a^2 r(x, y)^2} \rho(x, y)^{\frac{\gamma}{2}-1}, \\ v(x, y) = -ax \sqrt{\frac{\gamma}{2}} e^{-a^2 r(x, y)^2} \rho(x, y)^{\frac{\gamma}{2}-1}, \end{cases} \quad (4.10)$$

with $a = 8$. Note that this exact stationary solution is well-prepared, with a divergence-free velocity field.

For $M = 1$, the space domain is $(0, 1)^2$; for $M = 10^{-1}$, the space domain is $(0, 2)^2$. We prescribe periodic boundary conditions since the solution is constant at the boundaries. In both cases, we take $\xi = \frac{1}{100}$, and the final time is $t_{\text{end}} = 0.05\sqrt{M}$. The solution computed with our MOOD3(4) scheme for $M = 1$ on a 250×250 grid is displayed in Figure 10.

The error lines for $M = 1$ and $M = 10^{-1}$ are respectively reported in Figures 11 and 12. We note that, for $M = 10^{-1}$, the IMEX1 method has trouble converging. However, on this smooth solution, the MOOD method has not been activated at all. This confirms the fact that the detection criterion based on the Riemann invariants is able to correctly detect smooth regions, and to appropriately keep the high-order schemes when they do not oscillate. As a consequence, the TVD-MOOD scheme remains third-order accurate for each value of the Mach number M under consideration. Furthermore, we see from the errors that the diffusion is independent of the Mach number, and since the initial condition is well-prepared it is a strong indication that the scheme is also asymptotic preserving.

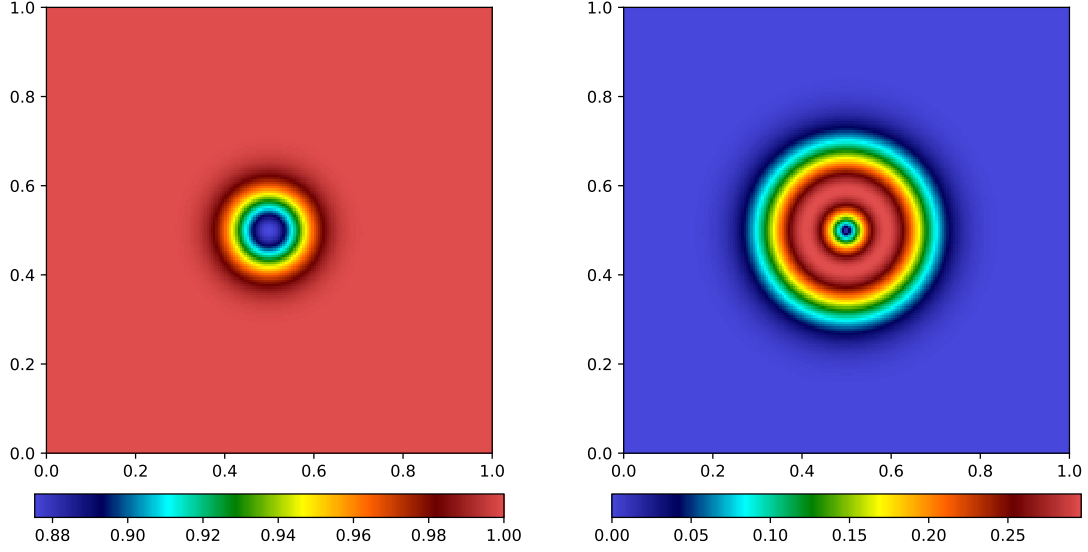


FIGURE 10. Bidimensional vortex (4.10) of the isentropic Euler equations: Density ρ (right panel) and norm of the momentum $\|\rho\mathbf{u}\|$ (left panel) obtained with MOOD3(4) on a 250×250 mesh for $M = 1$.

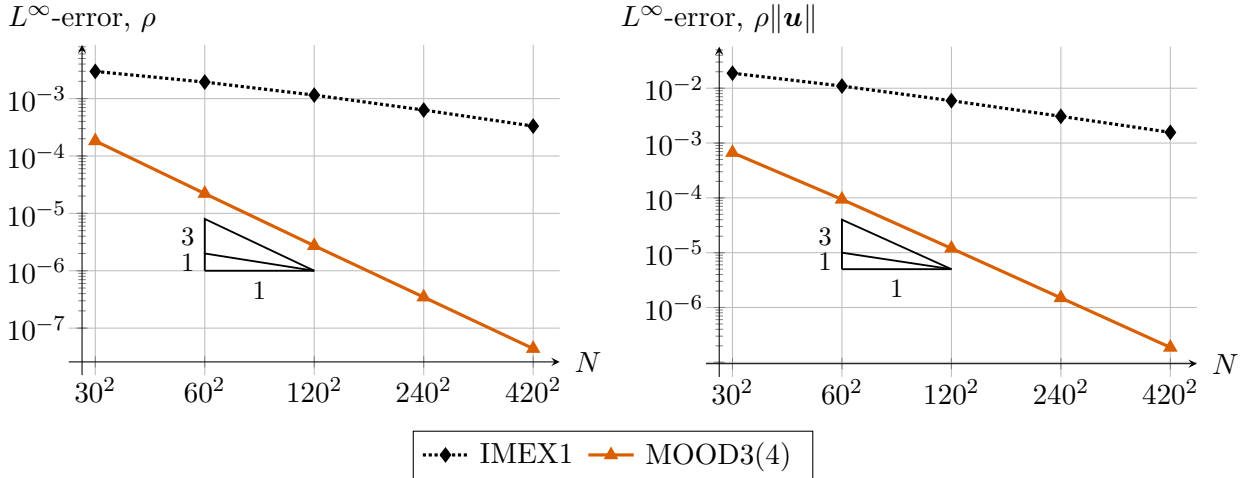


FIGURE 11. Error lines in L^2 norm for the 2D vortex described in Section 4.2.3, with $M = 1$, using the IMEX1 and MOOD3(4) schemes. Left panel: errors on the density ρ ; right panel: errors on the momentum norm $\|\rho\mathbf{u}\|$.

5. Conclusions and future work

We have presented a new approach to construct first order TVD IMEX-RK schemes which are suitable as MOOD parachute schemes to simulate multi-scale equations. Their development is motivated by the fact that there is a first order barrier for unconditionally stable implicit TVD schemes, as well as IMEX-TVD schemes that have a CFL condition which is only restricted by material wave velocities. We introduced a new class of TVD schemes consisting in a convex combination of a first-order TVD IMEX

TVD-MOOD SCHEMES

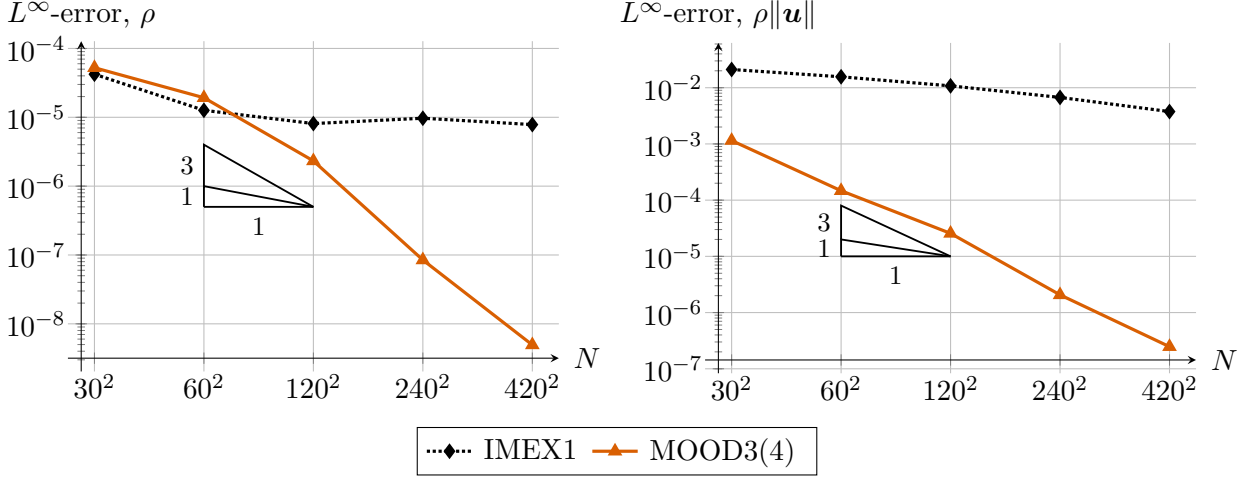


FIGURE 12. Error lines in L^2 norm for the 2D vortex described in Section 4.2.3, with $M = 10^{-1}$, using the IMEX1 and MOOD3(4) schemes. Left panel: errors on the density ρ ; right panel: errors on the momentum norm $\rho\|\mathbf{u}\|$.

scheme with a high-order IMEX RK scheme. We gave a theoretical justification of our TVD approach by means of studying a one dimensional linear scalar equation. This overall first order scheme is then used as a parachute scheme in a MOOD procedure with high order IMEX-RK schemes. Consequently, whenever the TVD property is violated, the parachute scheme is activated, ensuring the TVD property. This was verified by a discontinuous solution for scalar linear transport, see Figure 4, as well as for Riemann problems for the isentropic Euler equations, see Figures 6, 7, 8, 9 in one and two space dimension and in different Mach number regimes. Further, it was verified that the MOOD procedure yields high order convergence for smooth solutions for a smooth stationary two dimensional vortex, see Figures 11, 12 for different Mach numbers. Our results are a significant improvement to the scheme from [11] for isentropic Euler equations, especially for small Mach numbers. Furthermore, we numerically showed that using our IMEX-TVD scheme as a basis in the MOOD procedure consistently decreases the space-time error compared to using a standard backward forward Euler scheme, see Table 2.

One of the features of the scheme is its Mach number independent CFL constraint which allows to use large time steps even for small Mach numbers. In Table 1, we saw that our scheme performs well compared to standard TVD-IMEX schemes from the literature that have to enforce a Mach number CFL condition leading to very small time steps. This underlines the flexibility of our scheme with respect of the focus of the simulation.

Appendix A. On the incompatibility of BDF with TVD

Using for instance a second order Backward-Differencing-Formula (BDF), see [2], to approximate the implicit derivative, leads to

$$\frac{\partial w(x, t)}{\partial x} \approx \frac{1}{\Delta x} (3w_j - 4w_{j-1} + w_{j-2}), \quad (\text{A.1})$$

while the third-order BDF approximation is given by

$$\frac{\partial w(x, t)}{\partial x} \approx \frac{1}{\Delta x} \left(\frac{11}{6}w_j - 3w_{j-1} + \frac{3}{2}w_{j-2} - \frac{1}{3}w_{j-3} \right). \quad (\text{A.2})$$

Let us show the incompatibility of BDF with TVD, using the second-order BDF as an example. With (A.1) in the first step of the scheme (3.9), we get

$$w_j^{(2)} + \mu_\varepsilon \frac{a_{22}}{2} \left(3w_j^{(2)} - 4w_{j-1}^{(2)} + w_{j-2}^{(2)} \right) = w_j^n - \lambda a_{22} \Delta_j^n.$$

Following the proof (3.10), we have

$$\begin{aligned} \|w^n\|_\infty &\geq \max_j \left| \left(1 + \mu_\varepsilon \frac{3a_{22}}{2} \right) w_j^{(2)} - \mu_\varepsilon \frac{a_{22}}{2} \left(4w_{j-1}^{(2)} - w_{j-2}^{(2)} \right) \right| \\ &\geq \left(1 + \mu_\varepsilon \frac{3a_{22}}{2} \right) \|w^{(2)}\|_\infty - \mu_\varepsilon \frac{a_{22}}{2} \max_j \left| 4w_{j-1}^{(2)} - w_{j-2}^{(2)} \right| \end{aligned}$$

To complete this step we need

$$\max_j \left| 4w_{j-1}^{(2)} - w_{j-2}^{(2)} \right| \leq 4\|w^{(2)}\|_\infty - \|w^{(2)}\|_\infty \quad (\text{A.3})$$

which is a contradiction to the inverse triangular equation. Therefore using a second-order BDF does not lead to a TVD scheme. We can even extend this observation to a BDF of general order. As it is derived to match the Taylor series expansion up to an order p , its general form has alternating signs, and it can be written using $p+1$ coefficients $\kappa_i \geq 0$, $i = 0, \dots, p$, as in [2]

$$\frac{\partial w(x, t)}{\partial x} \approx \kappa_0 w_j - \kappa_1 w_{j-1} + \kappa_2 w_{j-2} - \dots + \kappa_p w_{j-p} \quad (\text{A.4})$$

for an approximation of order p , where we have taken an even p for the moment. We use the BDF described by (A.4) for the approximation of the implicit space derivative, and we find in the estimate for the L^∞ stability:

$$\begin{aligned} \|w^n\|_\infty &\geq \max_j \left| \left(1 + \mu_\varepsilon a_{22} \kappa_0 \right) w_j^{(2)} - \mu_\varepsilon a_{22} \left(\kappa_1 w_{j-1}^{(2)} - \kappa_2 w_{j-2}^{(2)} + \kappa_3 w_{j-3}^{(2)} - \dots - \kappa_m w_{j-m}^{(2)} \right) \right| \\ &\geq \left(1 + \mu_\varepsilon a_{22} \kappa_0 \right) \|w^{(2)}\|_\infty - \mu_\varepsilon a_{22} \max_j \left| \kappa_1 w_{j-1}^{(2)} - \kappa_2 w_{j-2}^{(2)} + \kappa_3 w_{j-3}^{(2)} - \dots - \kappa_m w_{j-m}^{(2)} \right| \\ &\geq \left(1 + \mu_\varepsilon a_{22} \kappa_1 \right) \|w^{(2)}\|_\infty - \mu_\varepsilon a_{22} \max_j \left| \kappa_1 w_{j-1}^{(2)} - \kappa_2 w_{j-2}^{(2)} \right| - \dots \\ &\quad - \mu_\varepsilon a_{22} \max_j \left| \kappa_{p-1} w_{j-p-1}^{(2)} - \kappa_p w_{j-p}^{(2)} \right|. \end{aligned}$$

Analogously to (A.3), to achieve the right estimate, the inverse triangular inequality would be violated. The case of an odd p also fails.

Appendix B. On non-CK IMEX schemes

Consider the following Butcher tableaux, defining an IMEX scheme in non-CK, non-ARS form:

$$\begin{array}{c|cccc} 0 & 0 & 0 & \cdots & 0 \\ \tilde{c}_2 & \tilde{a}_{21} & 0 & \cdots & 0 \\ \vdots & \vdots & \ddots & \ddots & \vdots \\ \tilde{c}_s & \tilde{a}_{s1} & \cdots & \tilde{a}_{s,s-1} & 0 \\ \hline & \tilde{b}_1 & \cdots & \tilde{b}_{s-1} & \tilde{b}_s \end{array} \quad \text{implicit:} \quad \begin{array}{c|cccc} c_1 & a_{11} & 0 & \cdots & 0 \\ c_2 & a_{21} & a_{22} & \cdots & 0 \\ \vdots & \vdots & \vdots & \ddots & \vdots \\ c_s & a_{s1} & a_{s2} & \cdots & a_{ss} \\ \hline & b_1 & b_2 & \cdots & b_s \end{array} \quad (\text{B.1})$$

We derive stability conditions analogous to Theorem 3.2 for this case where the first column of the implicit tableau is non-zero. After lengthy computations, we get the following result:

TVD-MOOD SCHEMES

Theorem B.1. *Let $\tilde{A}, A \in \mathbb{R}^{s \times s}$, $\tilde{b}, b, \tilde{c}, c \in \mathbb{R}^s$ define two Butcher tableaux (B.1) fulfilling (3.4) and the p -th order compatibility conditions. Let \tilde{b} and b coincide with the last rows of \tilde{A} and A respectively. For $k = 1, \dots, s$ and $l = 1, \dots, k - 1$, we define*

$$\mathcal{A}_k = \theta_k a_{kk} + (1 - \theta_k) c_k, \quad \tilde{\mathcal{A}}_k = (1 - \theta_k) \tilde{c}_k, \quad \mathcal{B}_{kl} = \frac{\theta_k a_{kl}}{\mathcal{A}_l}, \quad \tilde{\mathcal{B}}_{kl} = \theta_k \tilde{a}_{kl}.$$

In addition, we recursively define the following expressions:

$$\begin{aligned} \tilde{\mathcal{C}}_k &= \tilde{\mathcal{A}}_k - \sum_{l=2}^{k-1} \mathcal{B}_{kl} \tilde{\mathcal{C}}_l, & \tilde{\mathcal{D}}_{kl} &= \tilde{\mathcal{B}}_{kl} - \sum_{r=l+1}^{k-1} \mathcal{B}_{kr} \tilde{\mathcal{D}}_{rl}, \\ \mathcal{C}_k &= 1 - \sum_{l=1}^{k-1} \mathcal{B}_{kl} \mathcal{C}_l, & \mathcal{D}_{kl} &= \mathcal{B}_{kl} - \sum_{r=l+1}^{k-1} \mathcal{B}_{kr} \mathcal{D}_{rl}. \end{aligned}$$

Then, under the following restrictions for $k = 1, \dots, s$ and $l = 1, \dots, k - 1$,

$$\mathcal{A}_k > 0, \quad 0 \leq \lambda \tilde{\mathcal{C}}_k \leq \mathcal{C}_k, \quad 0 \leq \lambda \tilde{\mathcal{D}}_{k,l} \leq \mathcal{D}_{k,l},$$

the scheme consisting in the convex combination based on the Butcher tableaux (B.1), combined with a TVD limiter, is L^∞ stable and TVD under a CFL condition determined by $\lambda \geq 0$ where λ does not depend on ε .

When performing numerical experiments, we observe that the results of schemes derived under the conditions of Theorem B.1 are not as compelling as results of schemes obeying Theorem 3.2. Therefore, we do not include such schemes in the numerical experiments, but we still state Theorem B.1 for the sake of completeness.

Appendix C. TVD3(4)

For the TVD3(4) scheme, the explicit Butcher tableau is given by:

0	0	0	0	0
0.2049503677289891	0.2049503677289891	0	0	0
0.4173127343286904	0.2123925641886599	0.2049201701400305	0	0
0.9048203025659662	-0.4501877125339555	0.3955748607480934	0.9594331543518283	0
	0	0.3354718384287510	0.3487815573407456	0.3157466042305059

while the implicit Butcher tableau is given as follows:

0	0	0	0	0
0.2049503677289891	0	0.2049503677289891	0	0
0.4173127343286904	0	0.2040104873103189	0.2133022470183705	0
0.9048203025659662	0	0.3991926529002874	0.4115004113464103	0.0941272383192684
	0	0.3354718384287510	0.3487815573407456	0.3157466042305059

Acknowledgements

This work was started during the SHARK-FV conference (Sharing Higher-order Advanced Research Know-how on Finite Volume <http://www.SHARK-FV.eu/>) held in 2019. The authors would also like to thank Emmanuel Franck, Raphaël Loubère and Gabriella Puppo for fruitful discussions and comments.

Bibliography

- [1] E. Abbate, A. Iollo, and G. Puppo. An Implicit Scheme for Moving Walls and Multi-Material Interfaces in Weakly Compressible Materials. *Commun. Comput. Phys.*, 27(1):116–144, 2019.
- [2] U. M. Ascher and L. R. Petzold. *Computer Methods for Ordinary Differential Equations and Differential-Algebraic Equations*. SIAM: Society for Industrial and Applied Mathematics, 1998.
- [3] U. M. Ascher, S. J. Ruuth, and R. J. Spiteri. Implicit-explicit Runge-Kutta methods for time-dependent partial differential equations. *Appl. Numer. Math.*, 25(2-3):151–167, 1997. Special issue on time integration (Amsterdam, 1996).
- [4] G. Bispen, K. R. Arun, M. Lukáčová-Medvidová, and S. Noelle. IMEX large time step finite volume methods for low Froude number shallow water flows. *Commun. Comput. Phys.*, 16(2):307–347, 2014.
- [5] S. Boscarino, G. Russo, and L. Scandurra. All Mach Number Second Order Semi-implicit Scheme for the Euler Equations of Gas Dynamics. *J. Sci. Comput.*, 77(2):850–884, 2018.
- [6] F. Bouchut, E. Franck, and L. Navoret. A low cost semi-implicit low-Mach relaxation scheme for the full Euler equations. *J. Sci. Comput.*, 83(1):24, 2020.
- [7] C. Bresten, S. Gottlieb, Z. Grant, D. Higgs, D. I. Ketcheson, and A. Németh. Explicit strong stability preserving multistep Runge–Kutta methods. *Math. Comput.*, 86(304):747–769, 2017.
- [8] S. Clain, S. Diot, and R. Loubère. A high-order finite volume method for systems of conservation laws—Multi-dimensional Optimal Order Detection (MOOD). *J. Comput. Phys.*, 230(10):4028–4050, 2011.
- [9] S. Conde, S. Gottlieb, Z. J. Grant, and J. N. Shadid. Implicit and Implicit–Explicit Strong Stability Preserving Runge–Kutta Methods with High Linear Order. *J. Sci. Comput.*, 73(2-3):667–690, 2017.
- [10] P. Degond and M. Tang. All speed scheme for the low Mach number limit of the isentropic Euler equations. *Commun. Comput. Phys.*, 10(1):1–31, 2011.
- [11] G. Dimarco, R. Loubère, V. Michel-Dansac, and M.-H. Vignal. Second-order implicit-explicit total variation diminishing schemes for the Euler system in the low Mach regime. *J. Comput. Phys.*, 372:178–201, 2018.
- [12] G. Dimarco, R. Loubère, and M.-H. Vignal. Study of a New Asymptotic Preserving Scheme for the Euler System in the Low Mach Number Limit. *SIAM J. Sci. Comput.*, 39(5):A2099–A2128, 2017.
- [13] S. K. Godunov. A difference scheme for numerical solution of discontinuous solution of hydrodynamic equations. *Math. Sbornik*, 47:271–306, 1959.
- [14] S. Gottlieb. On high order strong stability preserving Runge-Kutta and multi step time discretizations. *J. Sci. Comput.*, 25(1-2):105–128, 2005.
- [15] S. Gottlieb, D. Ketcheson, and C.-W. Shu. *Strong Stability Preserving Runge-Kutta and Multistep Time Discretizations*. WORLD SCIENTIFIC, 2011.

TVD-MOOD SCHEMES

- [16] S. Gottlieb and C.-W. Shu. Total variation diminishing Runge-Kutta schemes. *Math. Comp.*, 67(221):73–85, 1998.
- [17] S. Gottlieb, C.-W. Shu, and E. Tadmor. Strong stability-preserving high-order time discretization methods. *SIAM Rev.*, 43(1):89–112, 2001.
- [18] H. Guillard and C. Viozat. On the behaviour of upwind schemes in the low Mach number limit. *Comput. & Fluids*, 28(1):63–86, 1999.
- [19] A. Harten. On a Class of High Resolution Total-Variation-Stable Finite-Difference Schemes. *SIAM J. Numer. Anal.*, 21(1):1–23, 1984.
- [20] Ph. Helluy, O. Hurisse, and L. Quibel. Assessment of numerical schemes for complex two-phase flows with real equations of state. *Comput Fluids*, 196:104347, jan 2020.
- [21] I. Higueras. Strong Stability for Additive Runge–Kutta Methods. *SIAM J. Numer. Anal.*, 44(4):1735–1758, 2006.
- [22] I. Higueras, N. Happenhofer, O. Koch, and F. Kupka. Optimized strong stability preserving IMEX Runge–Kutta methods. *J. Comput. Appl. Math.*, 272:116–140, 2014.
- [23] I. Higueras, D. I. Ketcheson, and T. A. Kocsis. Optimal Monotonicity-Preserving Perturbations of a Given Runge–Kutta Method. *J. Sci. Comput.*, 76(3):1337–1369, 2018.
- [24] X. Y. Hu, N. A. Adams, and C.-W. Shu. Positivity-preserving method for high-order conservative schemes solving compressible Euler equations. *J. Comput. Phys.*, 242:169–180, 2013.
- [25] C. A. Kennedy and M. H. Carpenter. Additive Runge–Kutta schemes for convection–diffusion–reaction equations. *Appl. Numer. Math.*, 44(1-2):139–181, 2003.
- [26] S. Klainerman and A. Majda. Singular limits of quasilinear hyperbolic systems with large parameters and the incompressible limit of compressible fluids. *Comm. Pure Appl. Math.*, 34(4):481–524, 1981.
- [27] R. Klein. Scale-Dependent Models for Atmospheric Flows. *Annu. Rev. Fluid. Mech.*, 42(1):249–274, 2010.
- [28] R. J. LeVeque. *Numerical methods for conservation laws*. Lectures in Mathematics ETH Zürich. Birkhäuser Verlag, Basel, second edition, 1992.
- [29] W. H. Matthaeus and M. R. Brown. Nearly incompressible magnetohydrodynamics at low Mach number. *Phys. Fluids*, 31(12):3634, 1988.
- [30] G. Métivier and S. Schochet. The incompressible limit of the non-isentropic Euler equations. *Arch. Ration. Mech. Anal.*, 158(1):61–90, 2001.
- [31] V. Michel-Dansac, C. Berthon, S. Clain, and F. Foucher. A well-balanced scheme for the shallow-water equations with topography or Manning friction. *J. Comput. Phys.*, 335:115–154, 2017.
- [32] V. Michel-Dansac, C. Berthon, S. Clain, and F. Foucher. A two-dimensional high-order well-balanced scheme for the shallow water equations with topography and Manning friction. *Comput. & Fluids*, 230:105152, 2021.

- [33] V. Michel-Dansac and A. Thomann. On high-precision L^∞ -stable IMEX schemes for scalar hyperbolic multi-scale equations. In *Proceedings of NumHyp 2019*, SEMA SIMAI Springer Series. Springer International Publishing, 2019.
- [34] S. Noelle, G. Bispen, K. R. Arun, M. Lukáčová-Medvidová, and C.-D. Munz. A weakly asymptotic preserving low Mach number scheme for the Euler equations of gas dynamics. *SIAM J. Sci. Comput.*, 36(6):B989–B1024, 2014.
- [35] L. Pareschi and G. Russo. Implicit-explicit Runge-Kutta schemes for stiff systems of differential equations. In *Recent trends in numerical analysis*, volume 3 of *Adv. Theory Comput. Math.*, pages 269–288. Nova Sci. Publ., Huntington, NY, 2001.
- [36] L. Pareschi and G. Russo. Implicit-Explicit Runge-Kutta schemes and applications to hyperbolic systems with relaxation. *J. Sci. Comput.*, 25(1-2):129–155, 2005.
- [37] P.L. Roe. Generalized formulation of TVD Lax-Wendroff schemes. *ICASE NASA Langley Research Center, Hampton, VA*, ICASE Report No 84-53, 1984.
- [38] B. Schmidtman, B. Seibold, and M. Torrilhon. Relations between WENO3 and third-order limiting in finite volume methods. *J. Sci. Comput.*, 68(2):624–652, 2015.
- [39] C.-W. Shu and S. Osher. Efficient implementation of essentially nonoscillatory shock-capturing schemes. *J. Comput. Phys.*, 77(2):439–471, 1988.
- [40] J. A. Smoller and J. L. Johnson. Global solutions for an extended class of hyperbolic systems of conservation laws. *Arch. Ration. Mech. Anal.*, 32(3), 1969.
- [41] M. N. Spijker. Contractivity in the numerical solution of initial value problems. *Numer. Math.*, 42(3):271–290, oct 1983.
- [42] P. K. Sweby. High resolution schemes using flux limiters for hyperbolic conservation laws. *SIAM J. Numer. Anal.*, 21(5):995–1011, 1984.